

Coupled Model Simulations of Boreal Summer Intraseasonal
(30-50 day) Variability, Part 1: Systematic Errors and Caution on
Use of Metrics

K. R. Sperber¹ and H. Annamalai²

¹Program for Climate Model Diagnosis and Intercomparison
Lawrence Livermore National Laboratory
P.O. Box 808, L-103
Livermore, CA 94550 USA
(sperber1@llnl.gov)

²International Pacific Research Center/SOEST
University of Hawaii
1680 East West Road
Honolulu, HI 96822 USA

Climate Dynamics
January 2008
(in press)

Abstract

Boreal summer intraseasonal (30-50 day) variability (BSISV) over the Asian monsoon region is more complex than its boreal winter counterpart, the Madden-Julian oscillation (MJO), since it also exhibits northward and northwestward propagating convective components near India and over the west Pacific. Here we analyze the BSISV in the CMIP3 and two CMIP2+ coupled ocean-atmosphere models. Though most models exhibit eastward propagation of convective anomalies over the Indian Ocean, difficulty remains in simulating the life cycle of the BSISV, as few represent its eastward extension into the western/central Pacific. As such, few models produce statistically significant anomalies that comprise the northwest to southeast tilted convection which results from the forced Rossby waves that are excited by the near-equatorial convective anomalies. Our results indicate that it is a necessary, but not sufficient condition, that the locations the time-mean monsoon heat sources and the easterly wind shear be simulated correctly in order for the life cycle of the BSISV to be represented realistically.

Extreme caution is needed when using metrics, such as the pattern correlation, for assessing the fidelity of model performance, as models with the most physically realistic BSISV do not necessarily exhibit the highest pattern correlations with observations. Furthermore, diagnostic latitude-time plots to evaluate the northward propagation of convection from the equator to India and the Bay of Bengal also need to be used with caution. Here, incorrectly representing extratropical-tropical interactions can give rise to “apparent” northward propagation when none exists in association with the eastward propagating equatorial convection. It is necessary to use multiple cross-checking diagnostics to demonstrate the fidelity of the simulation of the BSISV.

Keywords: tropical intraseasonal variability, Madden-Julian oscillation, Asian Summer Monsoon, model intercomparison, metrics

1 Introduction

Relative to the boreal winter Madden-Julian oscillation (MJO; Madden and Julian 1971, 1972, 1994), the analysis of simulations of boreal summer intraseasonal (30-50 day) variability (BSISV) over the Indian/west Pacific monsoon region has received much less attention (Slingo et al. 2005). The BSISV has a more complex structure compared to the wintertime MJO, in which eastward propagation dominates, by also exhibiting northward propagation of convective anomalies over India (Yasunari 1979, 1981; Sikka and Gadgil 1980), and northwest propagation over the tropical west Pacific (Murakami et al. 1984). Such complex propagations result in regional heat sources and sinks (Annamalai and Slingo 2001), in particular a northwest to southeast tilted rainband (e.g., Fig. 5f). Theoretical (Lau and Peng 1990, Wang and Xie 1997) and observational studies (Annamalai and Slingo 2001, Kemball-Cook and Wang 2001, Lawrence and Webster 2002, Annamalai and Sperber 2005) indicate that the tilted rainband arises due to a Kelvin wave/Rossby wave interaction. Using a linear baroclinic model, Annamalai and Sperber (2005, hereafter referred to as AS05) confirmed that basic state easterly zonal wind shear is required for the forced Rossby waves to be established and give rise to the tilted rainband, consistent with the afore-mentioned theoretical works, and observational and general circulation model (GCM) sensitivity tests (Kemball-Cook and Wang 2001; Kemball-Cook et al. 2002). In agreement with the speculation of Annamalai and Slingo (2001), AS05 demonstrated the interactive nature of three main heating centers located over the equatorial central-eastern Indian Ocean, near India and the Bay of Bengal, and the tropical west Pacific. Thus, recent results of the evaluation of the 30-50 day mode during boreal summer have led us to the hypothesis that numerous necessary, though perhaps not sufficient, conditions for the simulation of the BSISV exist, including: (1) capturing the three main centers of precipitation in the time-mean state to provide for a mutually interactive monsoon system (2) climatological easterly wind shear over the Indian Ocean and west Pacific to provide an environment fa-

avorable for the emanation of Rossby waves, and (3) eastward propagation of equatorial intraseasonal convective anomalies to provide the required heating to produce a forced response that is then manifested as northward propagation of convective anomalies over India and their extension eastward over the Bay of Bengal. Of them, the eastward equatorial propagating component appears to be the primary pre-requisite, as will be demonstrated here.

Simulation of the eastward propagating MJO is a severe test of a model's ability to represent the tropical variability, and GCMs have been notorious in their inability to simulate the MJO (Slingo et al. 1996, Sperber et al. 1997, Sperber 2004, Liu et al. 2005, and Zhang et al. 2006). Recently, analyzing 7 of the 40 years of the available data, Lin et al. (2006) found that only half of the Coupled Model Intercomparison Project-3 (CMIP3) simulations used by the Intergovernmental Panel on Climate Change Fourth Assessment Report (IPCC AR4) exhibited coherent Kelvin and Rossby wave structures, and of those all but one had equivalent depths that were too deep, indicating phase speeds faster than observations. Using all 40 years of available CMIP3 data and an accepted methodology for isolating winters when observed MJO lead-lag relationships by the models are consistent with observations (Sperber et al. 2005, Sperber 2008 [in preparation]) finds that more than half of the models analyzed by Lin et al. (2006) can represent coherent eastward propagation of MJO convection over the Indian Ocean that subsequently extends into the western Pacific Ocean. Of the earlier generation CMIP2+ models, the European Centre-Hamburg (ECHAM4) family of coupled and uncoupled GCMs exhibit a realistic boreal winter MJO, especially in flux-adjusted configurations in which the time mean state of sea-surface temperature (SST) and low-level winds are in good agreement with observations (Sperber et al. 2005). Improved success in simulating the boreal winter MJO motivates us to determine if the CMIP3 and CMIP2+ models can also generate eastward propagating equatorial convection during the boreal summer. If so, they then may be able to capture the northward and northwest-

ward propagating components of the 30-50 day BSISV, provided the other necessary conditions mentioned above are reasonably represented.

Compared to the boreal winter MJO, attempts to simulate the BSISV have met with even poorer results (Sperber et al. 2001, Kang et al. 2002, and Waliser et al. 2003). The former work indicates that models had difficulty in representing the hierarchy of intraseasonal EOF's in the 850hPa wind field. The latter two works revealed that models typically fail to represent the eastward propagating equatorial convective anomalies (hereafter also referred to as equatorial component), and the intraseasonal northwest to southeast tilted rainband that are the hallmarks of the BSISV. Here, once again, coupled models using the ECHAM4 atmospheric GCM have shown promise in representing boreal summer northward propagation of convection over the Indian Ocean (Kemball-Cook et al. 2002, and Fu et al. 2003). Using ECHAM4 coupled to the University of Hawaii 2.5 layer intermediate ocean model, Kemball-Cook et al. (2002) noted that the intraseasonal variability over the western Pacific was deficient due to the poor climatological simulation of the easterly wind shear there in which the "observed northwestward propagation of convection is inhibited..." Over the Indian sector, where the simulated easterly wind shear is similar to observations, the northward propagation of convection was more realistic. Though the simulation of the BSISV in the ECHAM4 based coupled models exhibits sensitivity to the choice of ocean model, we will show that the simulated BSISV in these models is typically realistic, including the northwestward propagation over the tropical west Pacific. Rajendran et al. (2004) and Rajendran and Kitoh (2006) determined that air-sea interaction was essential for capturing many aspects of the life cycle of the BSISV, including amplitude and phase, by comparing coupled and uncoupled simulations with Meteorological Research Institute models. Seo et al. (2007) found that reducing SST time-mean biases by flux adjustment improves the ability to simulate the BSISV over the Indian Ocean.

In the present study, using the CMIP3 models and select simulations from CMIP2+, our focus is to assess the ability of the models to simulate the dominant mode of the BSISV, which is thought to result from an interaction between equatorial waves and the basic state. Observations indicate that about 78% of the northward propagating events over India are associated with the equatorial component (e.g., Lawrence and Webster 2002), and this stands out as the dominant mode of BSISV in various diagnostic analyses (Lau and Chan 1986; Annamalai and Slingo 2001; AS05). Our central hypothesis is that the simulation of the BSISV is dependent upon the models ability to capture the equatorial component together with a realistic time-mean basic-state in precipitation, SST, and zonal easterly shear. We will begin with an examination of the time-mean state in Section 3, and then demonstrate the ability of the models to simulate the eastward propagating equatorial component, the tilted rainband structure, and the north-northwest components over the Indian and west Pacific longitudes (Section 4). Due to the complex nature of BSISV, we will argue that using a multitude of diagnostics is necessary to convincingly demonstrate the fidelity of the BSISV simulation. For example, it will be shown that some traditional diagnostics (such as latitude-time lag plots) and metrics (such as pattern correlation and root-mean-square-differences [RMSD]), can be misleading when attempting to demonstrate the fidelity with which the BSISV is simulated by a model.

2 The Models, Observations, and Methods adopted

2.1 Models

Table 1 contains basic information regarding the coupled ocean atmosphere general circulation models used in this paper. We have examined the output of 15 CMIP3 simulations of the climate of the 20th Century (20c3m) that have been used in the IPCC AR4. These simulations attempt to replicate climate variations during the period ~1850-present by imposing each modelling groups best estimates of nat-

ural (e.g., solar irradiance, volcanic aerosols) and anthropogenic (e.g., greenhouse gases, sulfate aerosols, ozone) climate forcing during this period. For these models, data of sufficient temporal sampling (daily) to investigate intraseasonal variability were available for the 40-year period 1961-2000 (1961-1999 in the case of CCSM3). More detailed online model documentation for the CMIP3 models is available at:

http://www-pcmdi.llnl.gov/ipcc/model_documentation/ipcc_model_documentation.php

Two additional models from the CMIP2+ archive, ECHAM4/OPYC and ECHO-G, are also examined. For these models we analyze the same 20-year period used by Sperber et al. (2005) in their analysis of the boreal winter MJO. Very briefly, in ECHAM4/OPYC the atmospheric GCM was run at a horizontal resolution of T42, while in ECHO-G it was run at T30. In ECHAM4/OPYC the ocean GCM, version 3 of OPYC (Ocean and isoPYCnal coordinate), was also run at T42, but equatorward of 36° the meridional resolution gradually increases to 0.5° to better resolve equatorial ocean wave dynamics. In ECHO-G, the global Hamburg Ocean Primitive Equation Model (HOPE-G) was run at T42. Equatorward of $\pm 30^{\circ}$ the meridional resolution is gradually increased to 0.5° within 10 degrees of the equator to better resolve the equatorial wave guide. In both coupled models, annual-mean flux adjustment was incorporated to minimize drift of the coupled climate system in order to help maintain a realistic basic state. More details on the atmospheric and oceanic components used in these two coupled models are available in Roeckner et al. (1996), Oberhuber (1993a,b), Legutke and Maier-Reimer (1999), Legutke and Voss (1999), and Min et al. (2004).

2.2 Observations

For model validation, various observational data have been analyzed for June-September over the period 1979-95. The Advanced Very High Resolution Radiometer Outgoing Longwave Radiation

(AVHRR OLR) on the NOAA polar orbiting satellites has been used to identify the observed convective signature of the BSISV. These data have been daily averaged and processed on to a 2.5° latitude/longitude grid with missing values filled by interpolation (Liebmann and Smith 1996). This dataset has been used in a variety of MJO studies (e.g., Salby et al. 1994, Slingo et al. 1999, Sperber 2003) and is a reasonable proxy for tropical convection (Arkin and Ardanuy 1989). Monthly rainfall from the Climate Prediction Center Merged Analysis of Precipitation (CMAP; Xie and Arkin 1996), dynamical fields are from the NCEP/NCAR Reanalysis (Kalnay et al. 1996) and European Centre for Medium-Range Weather Forecasts Reanalysis (ERA40, Kallberg et al. 2005), and optimally interpolated SST from Reynolds and Smith (1994) are used.

2.3 Methods used

The spatio-temporal variability of intraseasonal OLR over the boreal summer monsoon region has been characterized by AS05 using cyclostationary empirical orthogonal function (CsEOF) analysis (see their Fig. 2). Succinctly, CsEOF analysis operates on the cyclicity of the covariance function to directly derive the space-time evolution for a user specified embedded period (Kim and North 1997). Kim and Wu (1999) compared CsEOF analysis with other techniques such as extended EOF, complex EOF, and principal oscillation pattern analysis. They found that CsEOF analysis captures the propagative features more realistically, in particular when the covariance of the given time series is cyclic in nature. For example, this technique has been successfully used to understand the propagative features of the ENSO (Kim 2003). However, a limitation of CsEOF analysis is that the stochastic undulation time series that is associated with the CsEOF is not useful for establishing interrelationships with other variables. Therefore, in order to obtain a principal component (PC) time series of variations associated with the observed BSISV we calculate the dot product of the daily patterns of 20-100 day

bandpass filtered AVHRR OLR with respect to the CsEOF pattern in Fig. 2d of AS05 (this pattern is denoted as day 0 since it is recovered as the leading mode in a conventional EOF analysis). For each day the dot product (projection) yields a principal component loading (hereafter referred to as PC-4). Similarly, the 20-100 bandpass filtered OLR from the models is projected onto the same observed CsEOF pattern to produce a PC-4 time series for each of the models. In this way the model-model-observational comparison is uniform since the model and observed data have all been projected onto the same observed basis function. With this technique the standard deviation of the respective PC's is a direct indication of the magnitude of the BSISV variations for each model. The respective PC-4 time series are then used for lead-lag regression to ascertain how well each of the models represent the observed BSISV. For each model we obtain the slopes and intercepts at each gridpoint for each time lag via linear regression back onto its 20-100 day filtered OLR anomalies. In order to present maps of convective anomalies in units of Wm^{-2} we scale the slopes by one standard deviation of their respective PC-4. Thus, the anomalies presented herein are for the case when PC-4 is strongly positive.

Additionally, we apply traditional diagnostics, such as lead/lag regression maps, latitude-time regression maps, and longitude-time regression maps, to evaluate the fidelity with which the BSISV is simulated and to suggest caution on their usage/interpretation. Animations of the BSISV life cycle from observations and the models are provided as supplemental material (<http://www-pcmdi.llnl.gov/projects/ken/>). As in Sperber et al. (1997), Sperber (2003), and Sperber et al. (2005), statistical significance is calculated assuming each pentad is independent, though for pattern correlation and RMSD calculations data at all gridpoints is used.

3 The Boreal Summer Time Mean State

As indicated in Section 1, a necessary condition for models to represent BSISV is to capture the time-mean climatology in precipitation, especially the three main centers of heating over Bay of Bengal, the western Pacific, the equatorial Indian Ocean, and the associated easterly wind shear in the vertical (200hPa - 850hPa). It is also important for the models to simulate the warm pool in the SST climatology and the associated surface specific humidity that are important for maintaining the equatorial waves (Salby et al. 1994; Wang and Xie 1997). An even more stringent test is that the models represent the mutual interaction of the major heat sources at intraseasonal time scales (AS05).

Figure 1 shows the June-September climatology of precipitation from observations and the models. Over the core monsoon region, 58.75°E-158.75°E, 11.25°S-28.75°N, where the observed time-mean precipitation is in excess of ~5 mm/day (Fig. 1a), one notes the three major heating centers. Within the major centers local maxima are observed to the west of regions of significant orography. Relative to the CMAP estimate over the core region, seven models (CGCM3.1(T47), CGCM3.1(T63), CSIRO Mk3.0, ECHAM4/OPYC, ECHO-G, ECHO-G (MIUB), and GFDL-CM2.1) have pattern correlations that equal or exceed 0.7 (Figs. 1c-d, f, h-j, and m). [In numerical weather prediction an anomaly correlation of 0.6 is the minimum level at which skill is suggested to be useful. However, for our purposes there is a physical basis for emphasizing models with pattern correlations of 0.7 or better. Though interannual variability is not investigated here, pattern correlations of climatological summer monsoon rainfall of 0.7 or better over the summer monsoon region were noted *a posteriori* for models that exhibited a realistic monsoon-ENSO teleconnection (Sperber and Palmer 1996 and Sperber et al. 2001). Importantly, Annamalai et al. (2007) found that *a priori* consideration of the quality of the mean-state precipitation was a necessity in establishing a realistic monsoon-ENSO teleconnection.] The pattern correlations, RMSD, and bias relative to CMAP rainfall are given in Table 2. Typically,

the RMSD is lower for models that have larger pattern correlations with CMAP rainfall. With the exception of ECHAM5/MPI-OM, all models have a dry bias compared to CMAP, with CSIRO Mk3.0 largest, despite a pattern correlation of 0.7. As noted in Annamalai et al. (2007), even though these seven models have similar pattern correlations, they show pronounced differences in capturing the three major centers of precipitation. Compared to CMAP rainfall (Fig. 1a), both versions of the CGCM3.1 model (Figs. 1c-d) do not adequately represent the equatorial Indian Ocean convection maximum, but they have a wet bias over the equatorial western Pacific. In contrast, GFDL-CM2.1 (Fig. 1m) has a wet bias over the equatorial Indian Ocean sector, but with a dry (wet) bias over the equatorial western Pacific Ocean (Maritime Continent). ECHO-G and ECHO-G (MIUB) [Figs. 1i-j] also tend to be too dry over the equatorial western Pacific Ocean, and they, like ECHAM4/OPYC (Fig. 1h) have a dry bias adjacent to the western Ghats. Even so, this latter model does produce the rainfall maxima over the three major centers of heating.

Models with lower pattern correlations (0.6 - 0.7) with CMAP rainfall (CCSM3.0, ECHAM5/MPI-OM, GFDL-CM2.0, IPSL-CM4, and MRI-CGCM2.3.2) typically have a deficiency in correctly simulating at least one of the three major convective centers. For example, too little rainfall is found along the monsoon trough and over continental India in IPSL-CM4 (Fig. 1o) while in CCSM3 the maximum rainfall is simulated over the western Indian Ocean instead of eastern Indian Ocean, along with a weakened monsoon over the tropical west Pacific (Fig. 1b). The MIROC3.2 models have the lowest pattern correlations since they do not capture both the tropical west Pacific and equatorial Indian Ocean rainfall patterns (Figs. 1p-q). From examining this large suite of models, the note of caution is that similar values of a pattern correlation do not necessarily reflect similar fidelity in representing observations.

Figure 2 shows the June-September climatology of SST (shaded) and the 1000hPa specific humidity (contours) from observations and the models. Climatological SSTs help determine the atmospheric convective instability and theoretical studies (e.g., Salby et al. 1994) suggest that the equatorial component amplifies over the warm pool due to larger availability of moist energy (specific humidity). As regards the simulation of the Indo-Pacific warm pool (SST > 28°C), most models capture the two maxima over the western and eastern near-equatorial Indian Ocean. Over the Maritime Continent and the western Pacific the SST pattern is less well simulated with many models exhibiting an equatorial cold tongue that penetrates too far west. The tendency is for such models to exhibit a split-Intertropical Convergence Zone in the western Pacific in the precipitation field (Fig. 1). The systematic model biases in the time-mean precipitation, particularly over the equatorial region, may have a direct bearing on the simulation of the BSISV. We will examine this in more detail in Section 4.

The relationship between SST and precipitation is a delicate balance of the suite of parameterizations employed within a model, including the choice of ocean model. Using the same atmospheric model (ECHAM4), Fu et al. (2002) have demonstrated improvement in the representation of the mean monsoon rainfall in coupled ocean-atmosphere simulations compared to forced SST runs, while coupling to different ocean models can result in biases in air-sea interaction that compromise the mean state and intraseasonal variability (Sperber et al. 2005). In observations the core monsoon region is where precipitation exceeds ~5 mm/day (Fig. 1a), and is coincident with SST that typically exceeds 28°C (Fig. 2a). In the models, however, such close correspondence between SST and precipitation does not exist. For example, both FGOALS-g_1.0 and IPSL_CM4 have a substantial dry bias in the simulation of precipitation compared to observations (Table 2), and they produce a warm bias in SST. Whether or not the warm bias in FGOALS-g_1.0 and IPSL_CM4 is due to lack of sufficient precipitation leading to more solar insolation that subsequently warms the sea surface, the mixed-layer heat

budget analysis necessary to address this question is beyond the scope of the present study. Conversely, despite a systematic cold bias in CNRM_CM3, intense precipitation occurs where SST is $\sim 26^{\circ}\text{C}$, and the dry bias in the simulated precipitation is not that large (Table 2). Stowasser and Annamalai (2008) note that in the climate change experiments deep convection occurs in regions of SST greater than 31°C in the GFDL_CM2.1 model. This implies that deep convection occurs in regions where SSTs are higher than in surrounding areas supporting the moist static energy budget analysis of Neelin and Held (1987). The inference is that the gradient of SST is important while a systematic cold bias in the simulated SST over the entire ASM region does not necessarily result in large systematic errors in the simulated precipitation.

Figure 3 shows the easterly shear from observations and models. Since the wind shear is a measure of the integrated heat source (first internal baroclinic mode; Webster and Yang 1992; Ferranti et al. 1997), it is our premise that it may not be as sensitive to the simulated regional biases in precipitation (Fig. 1). Both in observations and models, the easterly shear show a strong asymmetry with respect to the equator. The shear is prominent over the northern Indian Ocean and tropical west Pacific, and most models also capture the local maximum over the western Arabian Sea. In the models, however, there are differences in the strength, and the zonal and meridional extent of the shear.

Figures 1-3 highlight the strengths and weaknesses of the simulated time-mean basic state. From a large-scale point-of-view, it is encouraging that most models have a reasonable time-mean representation of equatorial SST, surface specific humidity, and easterly shear. Though these attributes are not sufficient conditions for the development of the BSISV they suggest that the background state is potentially favorable for BSISV development. From a regional perspective these attributes are best represented over the Indian Ocean. Thus, based on our hypothesis one would expect the simulation of BSISV over the Indian Ocean to be of higher quality than that over the western Pacific. Despite having

a large-scale time-mean environment that is favorable for the BSISV, it should be stressed here that unstable coupled modes at intraseasonal time scales owe their existence to atmospheric waves (Hirst and Lau 1990) that are then destabilized and modified by the basic state (Wang and Xie 1997), air-sea interaction (Sperber et al. 1997; Waliser et al. 1999), cloud-radiation (Hu and Randall 1995), and convection and water vapor feedbacks (Woolnough et al. 2000), among other factors. Thus, the mere representation of the time-mean basic state alone does not guarantee a realistic simulation of the BSISV.

4 Boreal Summer Intraseasonal Variability and Caution on use of Metrics

In this section, we present results obtained from a suite of diagnostics that illustrate the models' ability to simulate the convective signatures of the BSISV. Initially, gross measures of intraseasonal variability are presented, followed by the evaluation of key aspects of the life cycle of the BSISV, and the need to exercise caution when interpreting traditional BSISV metrics and diagnostics.

4.1 Variance Structure

In Fig. 4 we show the 20-100 day bandpass filtered OLR variance. These data include propagating and standing intraseasonal components, and as such this diagnostic is indicative of the basic intraseasonal structure captured by the models. Despite differences in the amplitude of the intraseasonal variance CSIRO Mk3.0, the ECHAM and GFDL models, and IPSL-CM4 (Figs. 4f-j, l-m, and o) have the most realistic spatial patterns. With the exception of ECHAM5/MPI-OM (Fig. 4g) all of the models fail to represent the intraseasonal variability that is directly adjacent to the western Ghats in observations (Fig. 4a). In most models the tendency is for local maxima in intraseasonal variance to be collocated with regions of time-mean precipitation maxima, consistent with observations (Fig. 1). However, in the case of CGCM3.1 (T47), CGCM3.1 (T63), and FGOALS-g1_0 (Figs. 4c-d, k), the intraseasonal

variance maxima occur mostly along the periphery of the large-scale rainfall pattern where the rainfall is about 3mm day^{-1} , and in the GISS-AOM model (Fig. 4n) intraseasonal variance is virtually nonexistent. Though these latter results suggest that realistic time-mean rainfall is not a sufficient condition for the simulation of the intraseasonal variance structure, the lack of the association between maxima in time-mean precipitation and intraseasonal variance suggests a fundamental problem of the manner in which precipitation variations are generated with respect to the large-scale environment. We now present more detailed diagnostics to further assess simulations of the BSISV.

4.2 Space-time evolution of the 30-50 day mode

Figure 5 shows the patterns obtained by linearly regressing the observed PC-4 on to the 20-100 day filtered AVHRR OLR at various time lags. Also given are the pattern correlations of each of the pentad regression patterns as compared to the CsEOF patterns in Fig. 2 of AS05. For day 0, the pattern on which the filtered OLR was projected to obtain PC-4, the pattern correlation is 0.96. At other time lags the pattern correlation is slightly lower, with the most substantial difference occurring at day -15, though the essential features seen in the CsEOF of AS05 are well represented. Importantly, the space-time evolution is also consistent with the CsEOF of 20-100 day filtered pentad CMAP rainfall (not shown) and the extended EOF patterns presented in Seo et al. (2007), emphasizing the consistency between rainfall and OLR over this domain.

At day -15 the onset of convection occurs over the western Indian Ocean with suppressed convective anomalies bifurcating poleward over the central-eastern Indian Ocean (Fig. 5a). The bifurcation is asymmetric, with the anomalies in the Northern Hemisphere being stronger than those in the Southern Hemisphere, consistent with the studies of Wang and Rui (1990), Annamalai and Slingo (2001), and Lawrence and Webster (2002). From day -10 through day 0 the enhanced convection prop-

agates eastward and amplifies over the Indian Ocean (Figs. 5b-d). Further east, the suppressed convection also becomes stronger, exhibiting eastward and lastly northwestward propagation over the western Pacific. On day 5 (Fig. 5e) the enhanced convection over the Indian Ocean bifurcates. On days 10 and 15 the tilted band of enhanced convection extends southeastward to the west Pacific (Figs. 5f-g), and by day 20 the enhanced convection is mostly concentrated in the tropical west Pacific. At this time the suppressed phase dominates over the Indian Ocean (Fig. 5h), heralding the initiation of the break monsoon over India (AS05). Next we present the ability of the models to capture the three components of the BSISV.

4.3 Equatorial mode

If the BSISV is viewed as a coupled Kelvin wave-Rossby wave interaction, the primary protagonist in the life cycle of the BSISV is the equatorial component. As seen in observations (Fig. 6a), 5°N - 5°S averaged longitude-time lag plots of PC-4 regressed against filtered OLR, convection develops near the western Indian Ocean and begins to amplify between 60°E - 90°E at about day -10. A secondary amplification occurs over the equatorial west Pacific at about day 15 before the signal ceases in the central Pacific Ocean on about day 25. Like the winter counterpart, there is a see-saw in convective signatures between the equatorial Indian and west Pacific oceans. Based on the time interval between the suppressed phases over the equatorial Indian Ocean one can infer a recurrent time scale of about 36-40 days for the equatorial mode in summer.

Waliser et al. (2003) examined the BSISV in a suite of AGCMs forced by observed SST and found that in all the models the magnitude of the convective anomalies was too low over the equatorial eastern Indian Ocean. As seen in Fig. 6, all of the models generate the eastward propagating equatorial component that originates in the western Indian Ocean, though in most models it ceases near the

120°E, unlike that observed. Barring FGOALS-g1_0, the coupled models produce a clear amplification of convective anomalies near 90°E, consistent with observations. Given that all of the models have easterly wind shear over the Indian Ocean (Fig. 3), this environment is favorable for the emanation of forced Rossby waves and the generation of convective anomalies that bifurcate into the subtropics, a key aspect of the BSISV. In several models the eastward propagation continues coherently into the western Pacific, similar to the observations, suggesting that these models exhibit MJO-like behavior in the deep tropics [CCSM3, CGCM3.1 (T47), CGCM3.1 (T63), ECHAM4/OPYC, MIROC3.2(hires), and MIROC3.2(medres); Figs. 6b-d, h, p-q]. The eastward propagating convection weakens near the Maritime Continent in observations, but more so in ECHAM5/MPI-OM, the ECHO-G models, and GFDL-CM2.0 (Figs. 6g, i-j, l) in which statistically significant convective anomalies cease near 120°E. In the ECHO-G models the convection reinitiates further east while in ECHAM5/MPI-OM that which subsequently develops propagates in from the central Pacific, in contrast to observations. The link between mean state errors in precipitation and the BSISV is strongest over the Maritime Continent and western Pacific, as the models that fail to exhibit or have irregular and/or weak eastward propagation all have a dry bias in over this region (5°S-5°N, 120°-160°E). The ECHAM family of models have the strongest convective signatures and a realistic recurrent time scale in the equatorial component, with ECHAM4/OPYC showing the best agreement with observations in terms of propagation and the magnitude of the anomalous convection (Fig. 6).

4.4 Northward component over India and Northwestward component over west Pacific

Figure 7 shows latitude-lag regressions of filtered OLR in the vicinity of India relative to PC-4. Plots such as this have been used to demonstrate northward propagation in observations (e.g., Yasunari 1979) and to infer the ability of models to simulate northward propagation (e.g., Gadgil and Srinivasan

1990, Fu et al. 2003, Jiang et al. 2004, Rajendran et al. 2004, Rajendran and Kitoh 2006). Since the data for latitude-time plots has been averaged in longitude, there are three possible scenarios by which northward propagation may appear in such plots (1) as in the case of the observed 30-50 day BSISV, the northward propagating component arises as the forced Rossby wave response to the equatorial eastward propagating component (Figs. 5c-g), (2) northward propagation associated with a standing mode over the Indian Ocean, or (3) tropical-extratropical interactions may give rise to apparent northward propagation. Here we seek to determine if northward propagation is present in the simulations, and if so, is it consistent with the observed BSISV.

In observations, Fig. 7a, the enhanced convective anomalies first develop near the equator at about day -10, subsequently amplifying and bifurcating asymmetrically poleward from day 0 to day 15, as also seen in the space-time regressions in Fig. 5. The poleward migration reaches to $\sim 20^{\circ}\text{N}$, resulting in the active/break phases of the Indian monsoon. Figures 5-7 demonstrate that even during boreal summer, the equatorial component is stronger than the poleward component. Figure 7a further illustrates that the recurrent time scale of the BSISV is about 40 days.

The poleward bifurcation is represented by only 11 of the models, despite the fact that all of the models have some qualitative representation of the equatorial component (Fig. 6). The remaining 6 models, CCSM3, CGCM3.1 (T47), CGCM3.1 (T63), FGOALS-g1_0, GISS-AOM, and IPSL-CM4 (Figs. 7b-d, k, n-o) do not represent the bifurcation. As noted earlier, CGCM3.1 (T47), CGCM3.1 (T63), FGOALS-g1_0, and GISS-AOM (Figs. 6c-d, k, and n) have the weakest equatorial component over the Indian Ocean, suggesting that the off-equatorial response requires the equatorial diabatic heating to be of sufficient magnitude to elicit a response. In CCSM3 the seasonal mean Indian Ocean heat source is incorrectly located in the western Indian Ocean north of the equator, and in IPSL-CM4 there is a pronounced dry bias over India (Figs. 1b and 1o).

It is essential to determine for the models if the poleward propagation originates as an extension from that near the equator or if it is due to tropical-extratropical interactions. To facilitate this, in Fig. 8 we show longitude-time lag plots of the regression of PC-4 with filtered OLR averaged between 15°N-20°N. This enables us to evaluate the propagation characteristics over the continental latitudes and their relation to the equatorial eastward propagation. As seen in observations, Fig. 8a, eastward propagation of enhanced convection occurs between 60°E-95°E from about day 5-25, subsequent to the eastward equatorial convective anomalies (Fig. 6a). The eastward propagation in the 15°N-20°N region from 60°E-95°E is symptomatic of the bifurcation and the northward spread of convection from the equatorial region, as confirmed in Figs. 5d-h. Conversely, westward propagation dominates from the central Pacific to 100°E, and west of about 45°E. In the models, a common error near 15°N-20°N is the incorrect simulation of westward propagation that originates over the tropical west Pacific and penetrates over the Indian Ocean sector. The most pronounced example in this respect is CSIRO Mk3.0 (Fig. 8f). Either by coincidence, or due to other unknown interactions in the model, the development of westward propagating convective anomalies between 15°N-20°N occurs just subsequent to the equatorial anomalies (Fig. 6f). These anomalies merge with those that developed near the equator, thus giving the appearance of northward propagation in the latitude-time lag plot (Fig. 7f). This behavior is clearly seen in the movie of its BSISV life cycle (http://www-pcmdi.llnl.gov/projects/ken/CSIRO_Mk3.0.gif). ECHAM5/MPI-OM and GFDL-CM2.0 (Figs. 8g and 8l) also exhibit a similar deficiency in their ability to simulate the link between the eastward and northward propagation.

Our results indicate that when used without additional diagnostics, the latitude-time lag plots do not provide conclusive evidence of northward propagation of convective anomalies from the equator. None of the models are particularly good at representing the observed behavior between 15°N-20°N, though ECHO-G, ECHO-G(MIUB), and ECHAM4/OPYC (to a lesser extent) are the most realistic in

representing the development of convection in this latitude band subsequent to that further south. MIROC3.2(hires) and MIROC3.2(medres) are not consistent with observations since the Indian Ocean and western Pacific convective anomalies occur in-phase with one another (Figs. 8p-q). It should be noted that westward propagating convective signals, in particular those that originate over the west Pacific and migrate all the way into the Indian subcontinent, are prominent at biweekly (10-20 day) and synoptic time scales (Annamalai and Slingo 2001).

The third component of the BSISV is the northwest migration over the tropical west Pacific (Fig. 5). The westward component of this migration is reflected in the 15°N-20°N longitude-time lag plot (Fig. 8). In observations this evolves from the eastward propagating equatorial convective anomalies that expand northwestward. This feature is most realistic in ECHAM4/OPYC, and to a lesser extent in the ECHO-G models (Figs. 8h-j). In CSIRO_Mk3.0, GFDL_CM2.1, and MRI-CGCM2.3.2 in-situ convective anomalies develop over the equatorial central/west Pacific and then move northwestward (Figs. 8f, m, and r). One hypothesis, to be explored in future work, is that convective anomalies over the equatorial Indian Ocean force Kelvin waves and the anomalous low pressure signal associated with them may trigger convection near the equator which in turn propagates west-northwestward over the tropical west Pacific.

4.5 The tilted rainband

A key feature of the BSISV is the tilted band of enhanced convection that extends from the Arabian Sea to the Maritime continent (Figs. 5f and 9a). Note that for models to capture this unique feature the equatorial mode must pass over the Maritime continent and reach the west Pacific while Rossby waves emanated over the equatorial Indian Ocean migrate over the northern Indian Ocean. To be more precise, if a model captures all the three components of the BSISV for right reasons then one can expect

a realistic representation of the tilted rainband. Waliser et al. (2003) showed that this structure was poorly represented in GCMs, and in many cases the tilt incorrectly ran from the southwest to the northeast. Thus, the ability of a model to represent this feature, shown in Fig. 9, is a key test of its ability to simulate the BSISV.

For the models we have searched through the regressions for time lags between -25 and 25 days in order to isolate the pattern that gives the highest pattern correlation with the observed day 10 tilted convective band. In Fig. 9 the numbers in the upper-right corner of the plots give the day of the best match if it occurs on other than day 10. For the majority of models the closest pattern match occurs within a day or two day 10. The pattern correlations relative to the observed day 10 CsEOF pattern are given in column 2 of Table 3. Relative to the Day 10 CsEOF pattern (AS05), all models have smaller pattern correlations than does the day 10 AVHRR lag regression pattern. Here again we note that pattern correlations can be misleading, as the ECHAM5/MPI-OM model exhibits the largest pattern correlation among the simulations, though it does not produce the tilted band of enhanced convection (Fig. 9g). Lack of the tilted rainband suggests that this model does not represent the Kelvin wave/Rossby wave interaction that gives rise to the tilted convective band. Its large pattern correlation arises due to the simulation of the below-normal OLR anomalies near India, and the above-normal OLR anomalies over the equatorial Indian Ocean and the western Pacific. Rather, ECHAM4/OPYC and ECHO-G (Figs. 9h and 9i) give the most realistic representation of the tilted convection. CSIRO Mk3.0, ECHO-G (MIUB) and GFDL_CM_2.1 (Figs. 9f, j, m) exhibit a quadrupole-like convective structure, but the equatorial mode does not coherently pass over the Maritime Continent (Figs. 6f, j, m). In CNRM-CM3 (Fig. 9e) the tilt is not as pronounced as in observations (Fig. 9a), and the above-normal OLR over the western Pacific is weaker than observed.

A more stringent analysis and robust estimator of model fidelity is to calculate the pattern correlation over the full BSISV life cycle using the best matching patterns for all pentads from day -15 through day 20, as indicated in column 3 of Table 3. For all models this skill metric improves compared to that from the evaluation of the tilted rainband alone. While ECHAM4/OPYC is one of 3 models with the largest pattern correlation of 0.72, the physical interpretation is that this model is the most realistic in its representation of the BSISV, as discussed throughout Section 4. Confirmation of this is given in Fig. 10 in which its BSISV life cycle is presented. The individual pentadal spatial patterns have lower pattern correlations with the observed CsEOF than do the AVHRR regressions in Fig. 5. Despite this, this model simulates the major elements of the BSISV, including the initiation of convection in the western Indian Ocean (Fig. 10a), its eastward extension and amplification over the eastern Indian Ocean (Figs. 10 b-d) the poleward bifurcation and development of the tilted rainband (Figs. 10e-g), and the northwestward propagation of convection over the western Pacific near the South China Sea (Fig. 10h). Thus, the indication remains that independent checks regarding the fidelity of the BSISV propagative features are essential over and above the space-time pattern correlations.

5 Discussion

A hierarchy of OLR-based convective diagnostics have been employed to analyze the BSISV in climate models. The diagnostics include (1) near-equatorial longitude-time plots to evaluate the eastward propagating component of the BSISV (Fig. 6), (2) latitude-time plots to evaluate the northward propagating component of the BSISV near India and the Bay of Bengal (Fig. 7), and (3) plots (Figs. 9-10) and movies (<http://www-pcmdi.llnl.gov/projects/ken/>) of the spatio-temporal evolution over the eastern hemisphere. With regard to item (2), the northward propagation, we determined that for the models additional evidence was required to ensure the northward propagation was present and intimately

linked to the equatorial eastward propagation. The additional evidence took the form of a longitude-time plot of convective anomalies over the continental latitudes (Fig. 8). The convective life cycle movies, generated with daily (though filtered) data, were particularly insightful for evaluating the space-time evolution of the BSISV in the models. Utilizing these diagnostics we summarize in Table 4 the ability of the models to capture 5 important attributes of the convective anomalies associated with the BSISV. These attributes are (a) eastward propagation over the equatorial Indian Ocean, (b) extension of the equatorial eastward propagation over the Maritime Continent, (c) northward propagation near India, (d) northwestward propagation over the west Pacific, and (e) the tilted rainband that extends from India through the Maritime Continent. Only 2 models, ECHAM4/OPYC model, and to a lesser extent the ECHO-G model, capture these 5 key elements of the BSISV life cycle.

Despite only 2 models being able to capture the 5 major features of the BSISV, our results clearly indicate that substantial progress has been made in the simulation of BSISV, especially in the ability to simulate equatorial eastward propagation over the Indian Ocean. Here we attempt to interpret our results within the context of the basic state highlighted in Section 3 and existing theoretical considerations. In the following discussion, we only consider the point of view that the mean state sets the environment within which the transient activity occurs. An alternative hypothesis, as yet uninvestigated, is that the transient activity feeds back onto the mean state, in which case the regional details of the mean state may be closely tied to the transients. We also discuss the relationship between boreal summer and boreal winter intraseasonal variability, and we comment on future investigations.

5.1 Role of the basic state for the existence of the BSISV

One of the salient results of the present study is the simulation of the primary prerequisite of the BSISV, namely the equatorial eastward propagating convective anomalies over the Indian Ocean by

all the models (Fig. 6). Importantly, most models correctly capture the amplification of convective anomalies over the eastern equatorial Indian Ocean. Over the equatorial Indian Ocean, as during boreal winter (e.g., Sperber et al. 2005), this could be ascribed to realistically simulating of the SST, and the associated moist energy there (Fig. 2) despite differences in the amplitude and spatial distribution of the simulated precipitation (Fig. 1).

A major problem with the models is sustaining the equatorial eastward propagation over the Maritime Continent and producing the secondary amplification over the equatorial west Pacific (Fig. 6). The shortcoming over the Maritime Continent may be related to problems in the simulation of the diurnal cycle of convection, land-sea breezes, and land surface processes. Over the western Pacific there is a close correspondence between the lack of eastward propagation and the presence of a dry bias in rainfall, and there are substantial errors in SST. Thus, as suggested by Sperber et al. (2005) for the boreal winter, an improved representation of the precipitation and SST climatology in the western Pacific, especially over the region (5°S - 5°N , 120° - 160°E), may improve the ability of the models to simulate the eastward extension of equatorial convective anomalies into this region, resulting in improvement in the simulation of the BSISV and the MJO. Rectification of the cold tongue and split ITCZ simulation errors in the tropical Pacific is an ongoing task that involves improving both the atmospheric and ocean model components, and because it also has implications for improvements to other time scales of variability (e.g. the El Nino/Southern Oscillation).

At intraseasonal time scales unstable coupled modes, tropical Rossby waves sources, basic state SST/moist energy interactions, and easterly shear, contribute to the trapping of the moist equatorial waves within the monsoon region. Theory and simple models suggest the northward propagation is associated with the generation of Rossby waves from an eastward moving equatorial heat source with easterly vertical shear, boundary layer moisture advection, and air-sea interaction contributing to the

poleward component of propagation (Drbohlav and Wang 2005). The importance of the easterly wind shear was underscored by AS05 who found that the growth of Rossby waves over the monsoon domain was inhibited in a linear baroclinic model in which easterly shear was absent, consistent with the conclusions of Lau and Peng (1990) and Wang and Xie (1997). The easterly shear is however an integrator of the total monsoon heat source, so though this large-scale field may be well-represented in models, it is the regional details of the underlying heat sources that must be improved, including the association of intraseasonal variability maxima with rainfall maxima.

In observations, the equatorial mode exists in all seasons with the model results suggesting that the convective anomalies must be of sufficient strength to excite the off-equatorial poleward propagating component. In a few models the northward propagating component is absent despite the equatorial mode and easterly shear being represented. This begs the question of why in these models the Rossby waves are apparently not emanated. Suggested weaknesses may include a poor representation of boundary layer physics, including frictional convergence, and time-mean descent (IPSL-CM4) and/or too weak/diffuse of an equatorial forcing (e.g., CCSM3).

The model results provide insight into understanding the BSISV in contrast to northward propagating intraseasonal convective events over the Indian longitudes that occur independent of eastward propagation along the equator. In both cases convective heating near the equator will give rise to a Rossby wave response (Annamalai and Sperber 2005) and due to the hemispheric asymmetry of the mean state northward propagation of enhanced convection is favored. The 30-50 day BSISV is the special case in which the equatorial convection is propagating eastward.

A few years ago the simulation of the life cycle of the BSISV was elusive, especially the northwest to southeast tilted rainband. Essential elements for the establishment of the tilted rainband structure of the BSISV include the mean-state vertical windshear that sets the environment within which

the forced Rossby waves emanate, the physics over the Maritime Continent, and the strength of the equatorial mode. In the suite of models analyzed here, only two captured the tilted rainband (Table 4). The diagnostics performed here suggest that of the afore-mentioned elements the lack of eastward propagation of convection over the Maritime Continent and west Pacific stands out as a clear systematic error in the coupled models. Further understanding and improving model physics over the Maritime Continent is a challenging task for a proper representation of boreal winter MJO (e.g., Slingo et al. 2005) as well as the BSISV. In summary, in Section 1 we proposed a set of three linked hypotheses as necessary conditions for the simulation of BSISV. From the suite of results presented (Figures 6-10 and Table 4), it appears that the models that portray the entire life cycle of the BSISV satisfy all three conditions.

Increased horizontal resolution has been shown to be beneficial to the simulation of transients during the Asian summer monsoon (Sperber et al. 1994). Another nearly universal shortcoming in the models is the poor simulation of intraseasonal variability adjacent (west) of the western Ghats. While Annamalai and Sperber (2005) did not highlight this heat source as a main contributor to the interactions that make up the BSISV, it is important to represent it from a regional perspective. With the typically coarse horizontal resolution of the models analyzed herein, $\sim 2^\circ \times 2^\circ$ in latitude and longitude, it is not surprising that poorly resolving the orographic effect of the mountains will compromise the simulations, at least in the time-mean. For the CGCM3.1, T63 shows superior performance in capturing the rainfall adjacent to the western Ghats compared to the T47 version of the model (Figs. 1c and 1d), and for MIROC3.2 the hires version better represents the rainshadow effects of the western Ghats than does the medres version (Figs. 1p and 1q). Though increased horizontal resolution can be beneficial improved model physics is of paramount importance.

5.2 Caution on Use of Metrics

Our analysis also demonstrates that traditional metrics (scalar quantities) of model performance, namely pattern correlation and RMSD, must be used with caution. This was most apparent for the simulation of the tilted rainband, where an erroneous conclusion regarding which model was the most realistic at simulating this important component of the BSISV could have been drawn (Section 4.2, Fig. 9). Furthermore, we have demonstrated that the latitude-time diagnostic, used for assessing the ability of a model to produce northward propagation, is suspect in its ability to conclusively demonstrate said propagation. We are not advocating the disuse of these metrics and diagnostics, but rather we urge caution in their use, with additional diagnostics and a physical evaluation/interpretation of model fidelity essential to the analysis procedure.

5.3 Summer versus Winter ISO

The eastward propagation of BSISV convection along the equator has the same characteristics as that associated with the boreal winter MJO. It is the change in the basic state between summer and winter that promotes the differences in the off-equatorial intraseasonal behavior between the two seasons. Given that an essential component of both the BSISV and the boreal winter MJO is the eastward propagating equatorial component, an interesting question is: Is there a direct relation between the ability to simulate the boreal winter MJO and the BSISV? In the models that Waliser et al. (2003) analyzed, there was a close correspondence between the strength of the summer and winter intraseasonal variability based on the variance of the spatial pattern of the dominant EOF's from the opposing seasons. In our study the models and observations were all projected onto the same basis function, and thus the standard deviation of PC-4 is a direct indication of the magnitude of the intraseasonal convective anomalies, and this key metric of model variability was used to scale the respective regressions pre-

sented herein for each of the models. In Fig. 11 we evaluate the temporal variability of the BSISV PC-4 vs. MJO PC-2 from the boreal winter. In the latter case we calculate the standard deviation of PC-2 obtained from projecting the 20-100 day filtered OLR from the models on to the observed EOF-2 boreal winter MJO pattern given in Fig. 2g of Sperber (2003). EOF-2 from the boreal winter was chosen, since like BSISV basis function, the variance over the Indian Ocean is the dominant aspect of the spatial pattern. Our results indicate that the standard deviation of the boreal summer intraseasonal temporal variability has a correlation of 0.96 and a regression slope of 0.95 with that in boreal winter. This indicates a nearly one-to-one correspondence between the strength of the summer and winter intraseasonal temporal variations, and suggests that improvement to either the boreal summer or boreal winter intraseasonal variability should result in a commensurate improvement in the complimentary season.

5.4 Future Research

We now have one model, the ECHAM4/OPYC model, that very closely represents the full life cycle of the spatio-temporal evolution of convection of the BSISV. In part II (in preparation) a more detailed evaluation of the BSISV life cycle in the ECHAM4/OPYC model is performed, including examination of the relationship between convection and air-sea interaction, the surface fluxes, and its vertical structure. With the successful simulation of the BSISV by the ECHAM4/OPYC model, it now becomes possible to explore predictability issues, such as the relationship between the BSISV and ENSO. For example, using 850hPa winds from reanalysis, Sperber et al. (2000) demonstrated a link between a higher order subseasonal mode of variability and ENSO, noting that the leading mode had no link to the boundary forcing. An important question for simulating monsoon extremes is whether the model can reproduce similar interactions/relationships. If so, the model may provide a framework for under-

standing the processes that modulate intraseasonal variability, and the weather extremes (and their predictability) associated with the intraseasonal variability.

Acknowledgments K. R. Sperber was supported under the auspices of the U.S. Department of Energy Office of Science, Climate Change Prediction Program by Lawrence Livermore National Laboratory under contract DE-AC52-07NA27344. H. Annamalai was supported by a Department of Energy grant DE-FG02-07ER6445. The authors acknowledge the helpful comments of the reviewers, and we thank the Max Planck Institute for Meteorology and the German Climate Computer Centre for the ECHAM4/OPYC and ECHO-G model data provided through the Program for Climate Model Diagnosis and Intercomparison (PCMDI) CMIP2+ database. We acknowledge the modeling groups, the PCMDI, and the WCRP's Working Group on Coupled Modelling (WGCM) for their roles in making available the WCRP CMIP3 multi-model dataset. Support of this dataset is provided by the Office of Science, U.S. Department of Energy.

References

- Annamalai H., Slingo JM (2001) Active/break cycles: Diagnosis of the intraseasonal variability over the Asian summer monsoon. *Clim Dynam* 18: 85-102
- Annamalai H., Sperber, KR 2005: Regional heat sources and the active and break phases of boreal summer intraseasonal (30-50 day) variability. *J Atmos Sci* 62: 2726-2748
- Annamalai H., Hamilton K, Sperber KR (2007) South Asian summer monsoon and its relationship with ENSO in the IPCC AR4 simulations. *J Clim* 20: 1071-1092
- Arkin PA, Ardanuy PE (1989) Estimating climatic-scale precipitation from space: A review. *J Clim* 2: 1229-1238
- Drbohlav HKL, Wang B (2005) Mechanism of the northward- propagating intraseasonal oscillation: Insights from a zonally symmetric model. *J Clim* 18: 952–972
- Ferranti L, Slingo JM, Palmer TN, Hoskins BJ (1997) Relations between interannual and intraseasonal variability diagnosed from AMIP integrations. *Q J R Meteorol Soc* 123: 1323-1357
- Fu X, Wang B, Li T (2002) Impacts of air-sea coupling on the simulation of mean Asian summer monsoon in the ECHAM4 model. *Mon Wea Rev* 130: 2889-2904
- Fu X, Wang B, Li T, McCreary JP (2003) Coupling between Northward-Propagating, Intraseasonal Oscillations and Sea Surface Temperature in the Indian Ocean. *J Atmos Sci* 60: 1733-1753
- Gadgil S, Srinivasan J (1990) Low frequency variation of tropical convergence zones. *Meteor Atmos Physics* 44: 119-132
- Hirst A, Lau KM (1990) Intraseasonal and interannual variability in coupled ocean-atmosphere models. *J Clim* 3: 713-725
- Hu Q, Randall DA (1995) Low-frequency oscillations in radiative-convective systems. Part II: An idealized model. *JAS* 52: 478-490

- Jiang X, Li T, Wang B (2004) Structures and mechanisms of the northward propagating boreal summer intraseasonal oscillation. *J Clim* 17: 1022-1039
- Kallberg P, Berrisford P, Hoskins B, Simmons A, Uppala S, Lamy-Thepaut S, Hine R (2005) ECMWF Re-Analysis Project Report Series 19. ERA-40 Atlas. European Centre for Medium-Range Weather Forecasts, Reading, England 191pp
- Kalnay E, and Co-authors (1996) The NCEP/NCAR 40-year Reanalysis Project. *Bull Amer Meteor Soc* 77: 437-471
- Kang I-S, and Coauthors, (2002) Intercomparison of the climatological variation of Asian summer monsoon precipitation simulated by 10 GCMs. *Clim Dynam* 19: 383-395
- Kemball-Cook S, Wang B (2001) Equatorial waves and air-sea interaction in the boreal summer intraseasonal oscillation. *J Clim* 14: 2923-2942
- Kemball-Cook S, Wang B, Fu X (2002) Simulation of the intraseasonal oscillation in the ECHAM-4 Model: The impact of coupling with an ocean model. *J Atmos Sci* 59: 1433-1453
- Kim KY (2003) Investigation of ENSO variability using cyclostationary EOFs of observational data. *Meteorol Atmos Phys* 81: 149-168
- Kim KY, North GR (1997) EOFs of harmonizable cyclostationary processes. *J Atmos Sci* 54: 2416-2427
- Kim KY, Wu Q (1999) A comparison study of EOF techniques: Analysis of nonstationary data with periodic statistics. *J Clim* 12: 185-199
- Lau KM, Chan PH (1986) Aspects of the 40-50 day oscillation during the northern summer as inferred from outgoing longwave radiation. *Mon Wea Rev* 114: 1354-1367
- Lau KM., Peng L (1990) Origin of low frequency (intraseasonal) oscillations in the tropical atmosphere. Part III: Monsoon dynamics. *J Atmos Sci* 47: 1443-1462

- Lawrence DM, Webster PJ (2002) The boreal summer intraseasonal oscillation: Relationship between northward and eastward movement of convection. *J Atmos Sci* 59: 1593-1606
- Legutke S, Maier-Reimer E (1999) Climatology of the HOPE-G global ocean general circulation model. Tech. Rep. No. 21, German Climate Computer Centre (DKRZ), Hamburg, Germany, 90pp
- Legutke S, Voss R (1999) The Hamburg atmosphere-ocean coupled circulation model ECHO-G. Tech. Rep. No. 18, German Climate Computer Centre (DKRZ), Hamburg, Germany, 62pp
- Liebmann B, Smith CA (1996) Description of a complete (interpolated) OLR dataset. *Bull Amer Meteor Soc* 77: 1275-1277
- Lin J-L, and Coauthors (2006) Tropical intraseasonal variability in 14 IPCC AR4 climate models. Part I: Convective signals. *J Clim* 19: 2665-2690
- Liu P, Wang B, Sperber KR, Li T, Meehl GA (2005) MJO in the NCAR CAM2 with the Tiedtke Convection Scheme. *J Clim* 18: 3007-3020
- Madden RA, Julian PR (1971) Detection of a 40-50 day oscillation in the zonal wind in the tropical Pacific. *J Atmos Sci* 28: 702-708
- Madden RA, Julian PR (1972) Description of global-scale circulation cells in the tropics with a 40-50 day period. *J Atmos Sci* 29: 1109-1123
- Madden RA, Julian PR (1994) Observations of the 40-50 day tropical oscillation-A review. *Mon Wea Rev* 122: 814-837
- Min S-K, Legutke S, Hense A, Kwon W-T (2004) Climatology and internal variability in a 1000-year control simulation with the coupled climate model ECHO-G. Tech. Rep. No. 2, Model and Data Group, Max Planck Institute for Meteorology, Hamburg, Germany, 67pp
- Murakami T, Nakazawa T, He J (1984) On the 40-50 day oscillation during the 1979 northern hemisphere summer. Part I: Phase propagation. *J Meteorol Soc Japan* 62: 440-468

- Neelin JD, Held IM (1987) Modeling tropical convergence based on the moist static energy budget. *Mon Wea Rev* 115: 3-12
- Oberhuber J (1993a) Simulation of the Atlantic circulation with a coupled sea ice - mixed layer - isopycnal general circulation model. Part I: model description. *J Phys Oceanogr* 22: 808-829
- Oberhuber J (1993b) The OPYC ocean general circulation model. Tech. Rep. No. 7, Deutsches Klimarechenzentrum GmbH, Hamburg, Germany, 127pp
- Rajendran K, Kitoh A (2006) Modulation of tropical intraseasonal oscillations by ocean-atmosphere coupling. *J Clim* 19: 366-391
- Rajendran K, Kitoh A, Arakawa O (2004) Monsoon low-frequency intraseasonal oscillation and ocean-atmosphere coupling over the Indian Ocean. *Geophys Res Lett* 31: L02210, doi:10.1029/2003GL019031
- Reynolds RW, Smith TM (1994) Improved global sea surface temperature analyses using optimum interpolation. *J Clim* 7: 929-948
- Roeckner E, Arpe K, Bengtsson L, Christoph M, Claussen M, Dumenil L, Esch M, Giorgetta M, Schlese U, Schulzweida U (1996) The atmospheric general circulation model ECHAM-4: model description and simulation of present-day climate. Rep. No. 218, Max Planck Institute for Meteorology, Hamburg, Germany, 90pp
- Salby ML, Garcia RR, Hendon HH (1994) Planetary-scale circulations in the presence of climatological and wave-induced heating. *J Atmos Sci* 51: 2344-2367
- Seo K-H, Schemm J-K, Wang W, Kumar A (2007) The boreal summer intraseasonal oscillation simulated in the NCEP climate forecast system: the effect of seas surface temperature. *Mon Wea Rev* 135: 1807-1827 (DOI: 10.1175/MWR3369.1)

- Sikka DR, Gadgil S (1980) On the maximum cloud zone and the ITCZ over Indian longitudes during the southwest monsoon. *Mon Wea Rev* 108: 179-195
- Slingo JM, Sperber KR, Boyle JS, Ceron J-P, Dix M, Dugas B, Ebisuzaki W, Fyfe J, Gregory D, Guerry J-F, Hack J, Harzallah A, Inness P, Kitoh A, Lau WK-M, McAvaney B, Madden R, Matthews A, Palmer TN, Park C-K, Randall D, Renno N (1996) Intraseasonal oscillations in 15 atmospheric general circulation models: Results from an AMIP diagnostic subproject. *Clim Dynam* 12: 325-357
- Slingo JM, Rowell DP, Sperber KR, Nortley F (1999) On the predictability of the interannual behaviour of the Madden-Julian Oscillation and its relationship with El Niño. *Q J R Meteorol Soc* 125: 583-609
- Slingo JM, Inness PM, Sperber KR (2005) Modelling, Chap. 11 in *Intraseasonal Variability in the Atmosphere-Ocean Climate System*, Praxis, Springer, Berlin Heidelberg. pp361-388
- Sperber KR (2003) Propagation and the vertical structure of the Madden-Julian oscillation. *Mon Wea Rev* 131: 3018-3037
- Sperber KR (2004) Madden-Julian variability in NCAR CAM2.0 and CCSM2.0. *Clim Dynam* 23: 259-278 (DOI 10.1007/s00382-004-0447-4)
- Sperber, KR, Palmer T (1996) Interannual tropical rainfall variability in general circulation model simulations associated with the atmospheric model intercomparison research. *J Clim* 9: 2727-2750
- Sperber KR, Hameed S, Potter GL, Boyle JS (1994) Simulation of the northern summer monsoon in the ECMWF model: Sensitivity to horizontal resolution. *Mon Wea Rev* 122: 2461-2481
- Sperber KR, Slingo JM, Inness PM Lau W.K.-M (1997) On the maintenance and initiation of the intraseasonal oscillation in the NCEP/NCAR reanalysis and in the GLA and UKMO AMIP simulations. *Clim Dynam* 13: 769-795

- Sperber KR, Slingo JM, Annamalai H (2000) Predictability and the relationship between subseasonal and interannual variability during the Asian summer monsoon. *Q J R Meteorol Soc* 126: 2545-2574
- Sperber KR, Brankovic C, Deque M, Fredericksen CS, Graham R, Kitoh A, Kobayashi C, Palmer T, Puri K, Tennant W, Volodin E (2001) Dynamical seasonal predictability of the Asian summer monsoon. *Mon Wea Rev* 129: 2226-2248
- Sperber KR, Gualdi S, Legutke S, Gayler V (2005) The Madden-Julian oscillation in ECHAM4 coupled and uncoupled general circulation models. *Clim Dynam* 25: 117-140
- Stowasser M, Annamalai H (2008) Response of the South Asian summer monsoon to global warming: mean and synoptic systems. *J Clim* (in press)
- Waliser DE, Lau KM, Kim J-H (1999) The influence of coupled sea surface temperatures on the Madden-Julian oscillation: A model perturbation experiment. *J Atmos Sci* 56: 333-358
- Waliser DE, and Coauthors (2003) AGCM simulations of intraseasonal variability associated with the Asian summer monsoon. *Clim Dynam* 21: 423-446
- Wang B, Rui H (1990) Synoptic climatology of transient tropical intraseasonal convection anomalies: 1975-1985. *Meteorol Atmos Phys* 44: 43-61
- Wang B, Xie X (1997) A model for the boreal summer intraseasonal oscillation. *J Atmos Sci* 54: 72-86
- Webster PJ, Yang S (1992) Monsoon and ENSO: Selectively interactive systems. *Q J R Meteorol Soc* 118: 877-926
- Woolnough SJ, Slingo JM, Hoskins BJ (2000) The relationship between convection and sea surface temperature on intraseasonal time scales. *J Clim* 13: 2086-2104
- Xie P, Arkin P (1996) Analyses of global monthly precipitation using gauge observations, satellite estimates, and numerical model predictions. *J Clim* 9: 840-858

- Yasunari T (1979) Cloudiness fluctuations associated with the Northern Hemisphere summer monsoon. *J Meteor Soc Japan* 57: 227-242
- Yasunari T (1981) Structure of an Indian monsoon system with around 40-day period. *J Meteor Soc Japan* 59: 336-354
- Zhang C, Dong M, Gualdi S, Hendon HH, Maloney ED, Marshall, A, Sperber, KR, Wang W (2006) Simulations of the MAdden-Julian oscillation in four pairs of coupled and uncoupled models. *Clim Dynam* 27: 573-592 (DOI 10.1007/s00382-006-0148-2)

Table 1. The CMIP3 models analyzed in this study are listed by modelling group, including their designations, and the horizontal and vertical resolution of the atmospheric and oceanic component models.

Note: ECHAM4/OPYC and ECHO-G are from the CMIP2+ database.

Modelling Group	Model Designation	AGCM Horizontal/ Vertical Resolution	OGCM Horizontal/ Vertical Resolution
National Center for Atmospheric Research	CCSM3.0	T85 L26	384x288 L32
Canadian Centre for Climate Modelling & Analysis	CGCM3.1(T47) CGCM3.1(T63)	T47 L31 T63 L31	192x96 L29 256x192 L31
Centre National de Recherches Météorologiques (Meteo-France)	CNRM-CM3	T42 L45	180x170 L33
CSIRO Atmospheric Research	CSIRO Mk3.0	T63 L18	1.875x0.925 L31
Max Planck Institute for Meteorology	ECHAM5/MPI-OM ECHAM4/OPYC ECHO-G	T63 L32 T42 L19 T30 L19	1.5x1.5 L40 T42 L11 T42 L20
Meteorological Institute of the University of Bonn, Meteorological Research institute of KMA, Model and Data Group	ECHO-G (MIUB)	T30 L19	T42 L20
Institute of Atmospheric Physics	FGOALS-g1.0	T42 L26	1x1 L16
Geophysical Fluid Dynamics Laboratory (NOAA)	GFDL-CM2.0 GFDL-CM2.1	N45 L24 N45 L24	1x0.33-1 L50 1x0.33-1 L50
Goddard Institute for Space Studies (NASA)	GISS-AOM	90x60 L12	90x60 L16
Institut Pierre Simon Laplace	IPSL-CM4	96x72 L19	2x2 L31
Center for Climate System Research (The University of Tokyo), National Institute for Environmental Studies, and Frontier Research Center for Global Change (JAMSTEC)	MIROC3.2(hires) MIROC3.2(medres)	T106 L56 T42 L20	T106 L48 256x192 L44
Meteorological Research Institute	MRI-CGCM2.3.2	T42 L30	2x0.5-2.5 L23

Table 2. June-September climatological precipitation pattern correlation, RMSD, and bias for 1961-99 relative to CMAP rainfall (1979-1995) for the region 58.75°E-158.75°E, 11.25°S-28.75°N

Model Designation	Pattern Correlation	RMSD	Bias (model-obs)
CCSM3.0	0.60	3.02	-0.71
CGCM3.1(T47)	0.73	2.60	-0.70
CGCM3.1(T63)	0.72	2.62	-0.59
CNRM-CM3	0.55	3.00	-0.22
CSIRO Mk3.0	0.70	3.07	-1.69
ECHAM5/MPI-OM	0.66	2.86	0.03
ECHAM4/OPYC	0.73	2.79	-0.43
ECHO-G	0.74	2.47	-0.49
ECHO-G (MIUB)	0.75	2.49	-0.66
FGOALS-g1.0	0.45	3.46	-1.32
GFDL-CM2.0	0.64	3.00	-0.60
GFDL-CM2.1	0.71	2.57	-0.15
GISS-AOM	0.57	3.10	-0.77
IPSL-CM4	0.61	3.33	-1.56
MIROC3.2(hires)	0.36	3.81	-0.49
MIROC3.2(medres)	0.43	3.52	-0.42
MRI-CGCM2.3.2	0.64	3.11	-0.96

Table 3. Space-time correlation for PC-4 regressed patterns of BSISV from models and observations relative to the CsEOF's for Day 10 (column 2), and for the full space-time pattern correlation for Day -15 through Day 20 in increments of 5 days over the region 40°E-180°W, 10°S-30°N (column 3). For each CsEOF the best matching pattern (in terms of spatial correlation) is found. Due to slightly different time scales in the models the day at which the best match occurs may not correspond to that of the CsEOF. Note: data at all gridpoints are used in the calculation of the pattern correlation

Model Designation	Pattern Correlation Day 10	Pattern Correlation Days -15 to 20
AVHRR	0.90	0.91
CCSM3.0	0.42	0.60
CGCM3.1(T47)	0.33	0.62
CGCM3.1(T63)	0.30	0.60
CNRM-CM3	0.28	0.61
CSIRO Mk3.0	0.32	0.59
ECHAM5/MPI-OM	0.66	0.72
ECHAM4/OPYC	0.54	0.72
ECHO-G	0.36	0.66
ECHO-G (MIUB)	0.61	0.71
FGOALS-g1.0	0.26	0.46
GFDL-CM2.0	0.56	0.69
GFDL-CM2.1	0.64	0.72
GISS-AOM	0.28	0.42
IPSL-CM4	0.65	0.66
MIROC3.2(hires)	0.28	0.55
MIROC3.2(medres)	0.34	0.58
MRI-CGCM2.3.2	0.58	0.68

Table 4. The ability of the models to capture the important aspects of the BSISV is indicated with either a yes (Y) or no (N). The most conclusive evidence of success in simulating these benchmarks in the life cycle of the BSISV is examination of the animations that are provided as supplementary material (<http://www-pcmdi.llnl.gov/projects/ken/>). (1) Equatorial mode over Indian Ocean corresponds to convective anomalies reaching $\sim 100^{\circ}\text{E}$ (see Fig. 6), (2) Equatorial mode over Maritime Continent corresponds to convective anomalies reaching $\sim 150^{\circ}\text{E}$ (see Fig. 6), (3) Northward mode over India corresponds to convective anomalies reaching $\sim 20^{\circ}\text{N}$ (see Fig. 7 and Fig. 9), (4) Northwest mode over the west Pacific corresponds to convective anomalies that propagate north-northwestward over the South China Sea near 20°N (see Fig. 8), and (5) Tilted Rain Band corresponds to convective anomalies that extend contiguously southeastward from India to the Maritime Continent (see Fig. 9).

Model Designation	Equatorial mode over Indian Ocean	Equatorial mode over Maritime Continent	Northward mode over India	Northwest mode over West Pacific	Tilted Rain Band
AVHRR	Y	Y	Y	Y	Y
CCSM3.0	Y	Y	N	N	N
CGCM3.1(T47)	Y	Y	N	N	N
CGCM3.1(T63)	Y	Y	N	N	N
CNRM-CM3	Y	N	Y	N	N
CSIRO Mk3.0	Y	N	N	N	N
ECHAM5/MPI-OM	Y	N	Y	N	N
ECHAM4/OPYC	Y	Y	Y	Y	Y
ECHO-G	Y	Y	Y	Y	Y
ECHO-G (MIUB)	Y	Y	Y	Y	N
FGOALS-g1.0	Y	N	N	N	N
GFDL-CM2.0	Y	N	Y	Y	N
GFDL-CM2.1	Y	N	Y	Y	N
GISS-AOM	Y	N	N	N	N
IPSL-CM4	Y	N	N	Y	N
MIROC3.2(hires)	Y	N	Y	N	N
MIROC3.2(medres)	Y	Y	Y	N	N
MRI-CGCM2.3.2	Y	N	N	N	N

Figure Captions

Fig. 1. June-September climatology of precipitation rate (mm day^{-1})

Fig. 3. June-September climatologies of sea-surface temperature climatology ($^{\circ}\text{C}$, shaded) and 1000hPa specific humidity (kg kg^{-1})

Fig. 3. June-September climatology of the easterly wind shear (m s^{-1}) between 200hPa and 850hPa. The contour interval is 8 ms^{-1}

Fig. 4. June-September variance of 20-100 day bandpass filtered outgoing longwave radiation [$(\text{W m}^{-2})^2$]

Fig. 5. Lag regressions of 20-100 day filtered AVHRR OLR anomalies (W m^{-2}) with PC-4. Lag regressions have been scaled by one standard deviation of PC-4. The pattern correlations with the Cseof's of Annamalai and Sperber (2005) are given in parentheses

Fig. 6. Longitude-lag regression plots of 5°N - 5°S averaged 20-100 day filtered OLR anomalies (W m^{-2}) with PC-4. Lag regressions have been scaled by one standard deviation of PC-4

Fig. 7. Latitude-time lag regression plots of 71.25°E - 83.75°E averaged 20-100 day OLR anomalies (W m^{-2}) with PC-4. Lag regressions have been scaled by one standard deviation of PC-4

Fig. 8. Longitude-lag regression plots of 15°N-20°N averaged 20-100 day filtered OLR anomalies ($W m^{-2}$) with PC-4. Lag regressions have been scaled by one standard deviation of PC-4

Fig. 9. Tilted convection and quadrupole structure based on best fit pattern correlation to the day 10 CsEOF ($W m^{-2}$). The day of maximum correlation is given for those models whose pattern match occurs on a day other than day 10 from the PC-4 lag regression with 20-100 day filtered OLR anomalies. Lag regressions have been scaled by one standard deviation of PC-4

Fig. 10. As Fig. 5 but for ECHAM4/OPYC

Fig. 11. Plotted is the ratio of the simulated to the observed standard deviation of the boreal summer intraseasonal variability (PC-4) versus that of the boreal winter MJO (PC-2). The black line is the linear regression fit to the data for which the slope is given

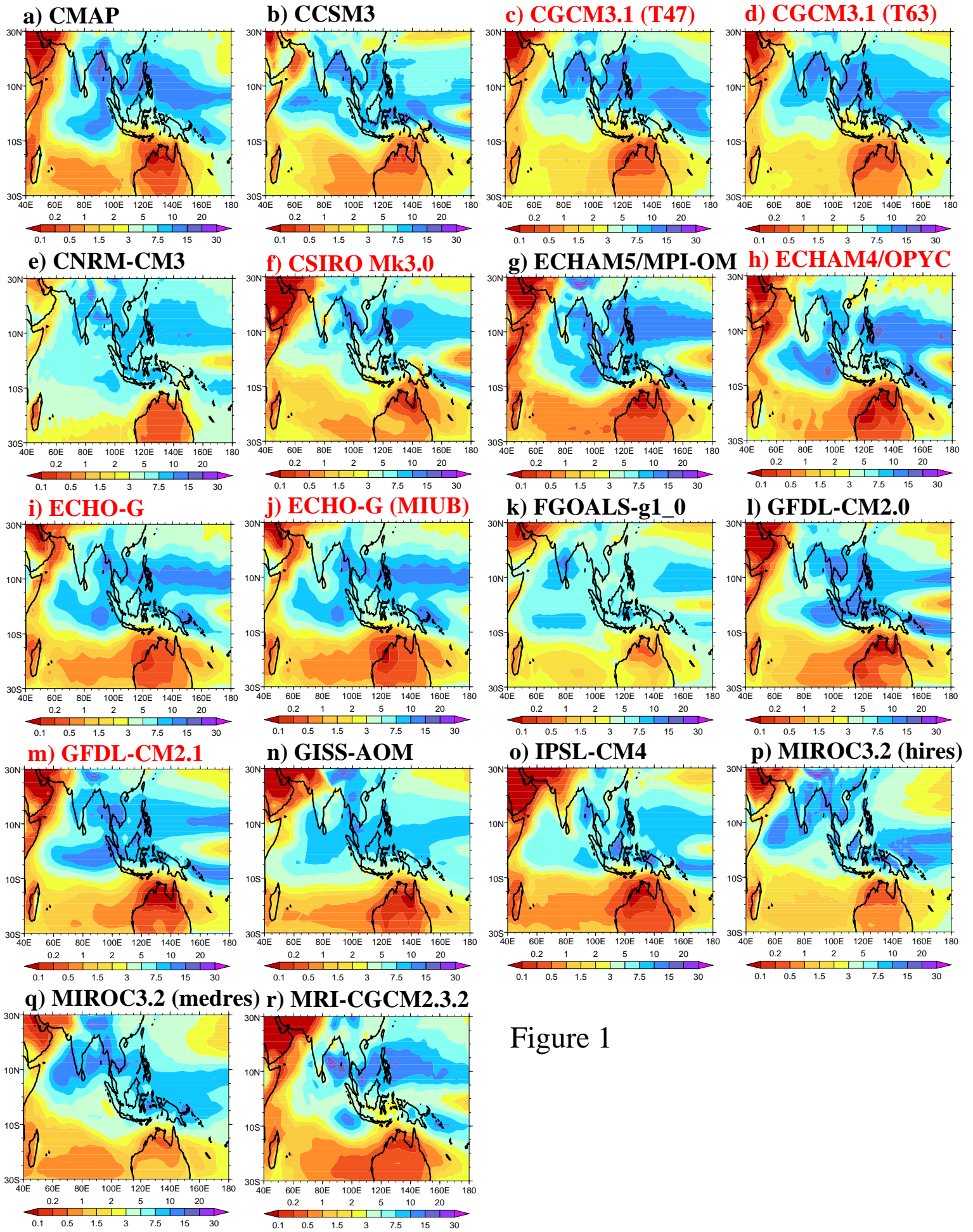


Figure 1

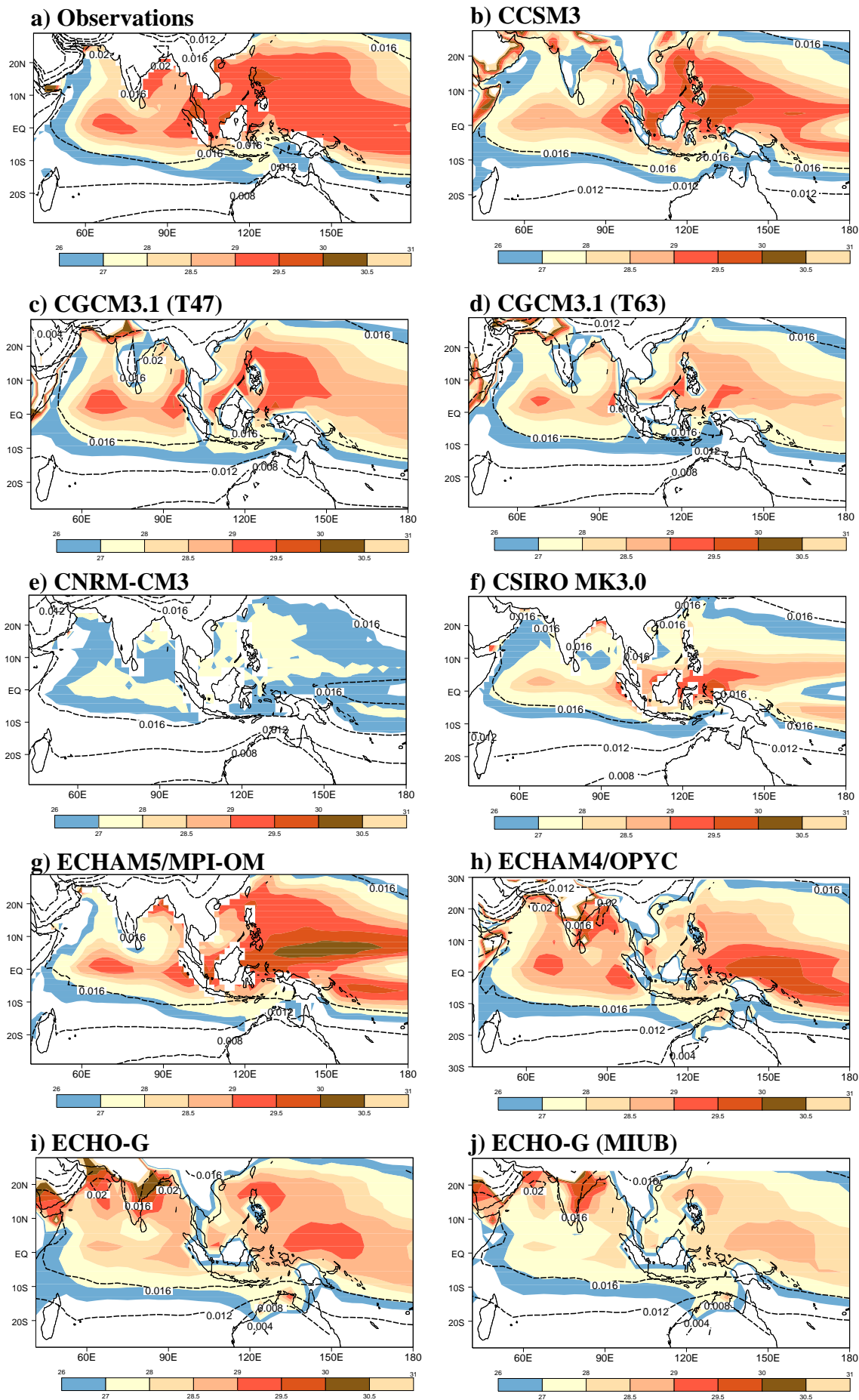
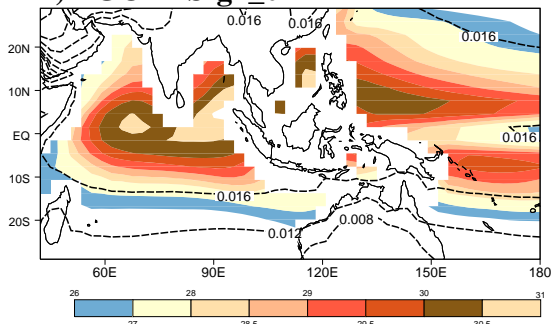
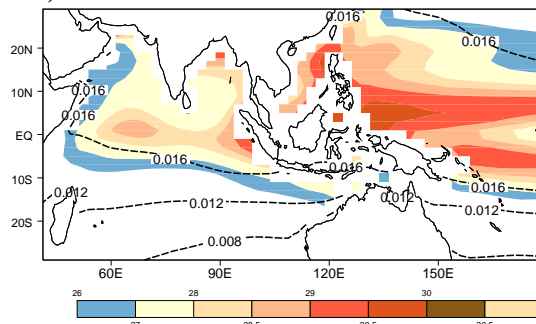


Figure 2

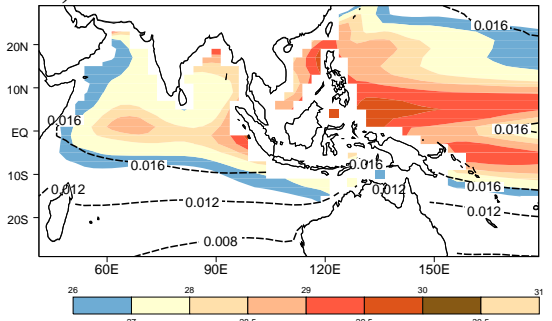
k) FGOALS-g1_0



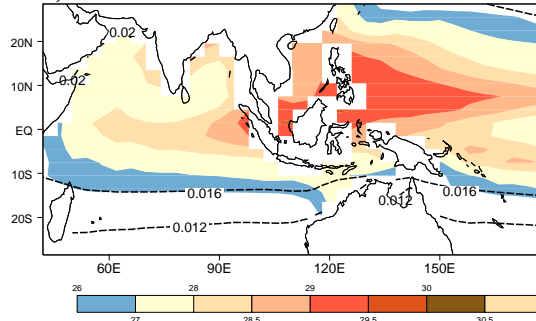
d) GFDL-CM2.0



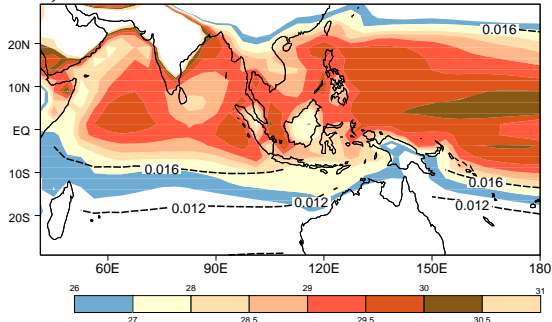
m) GFDL-CM2.1



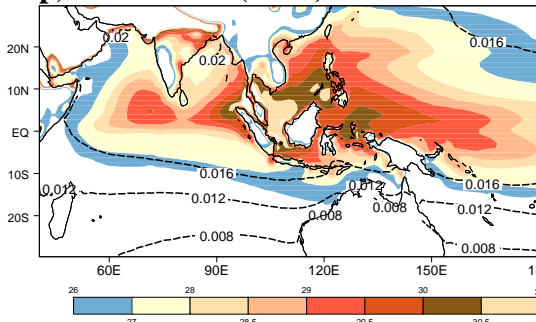
n) GISS-AOM



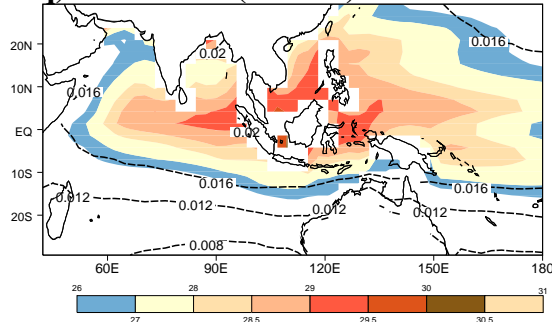
o) IPSL-CM4



p) MIROC3.2 (hires)



q) MIROC3.2 (medres)



r) MRI-CGCM2.3.2

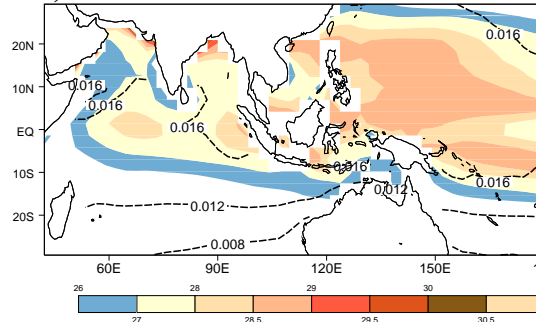


Figure 2 (con't)

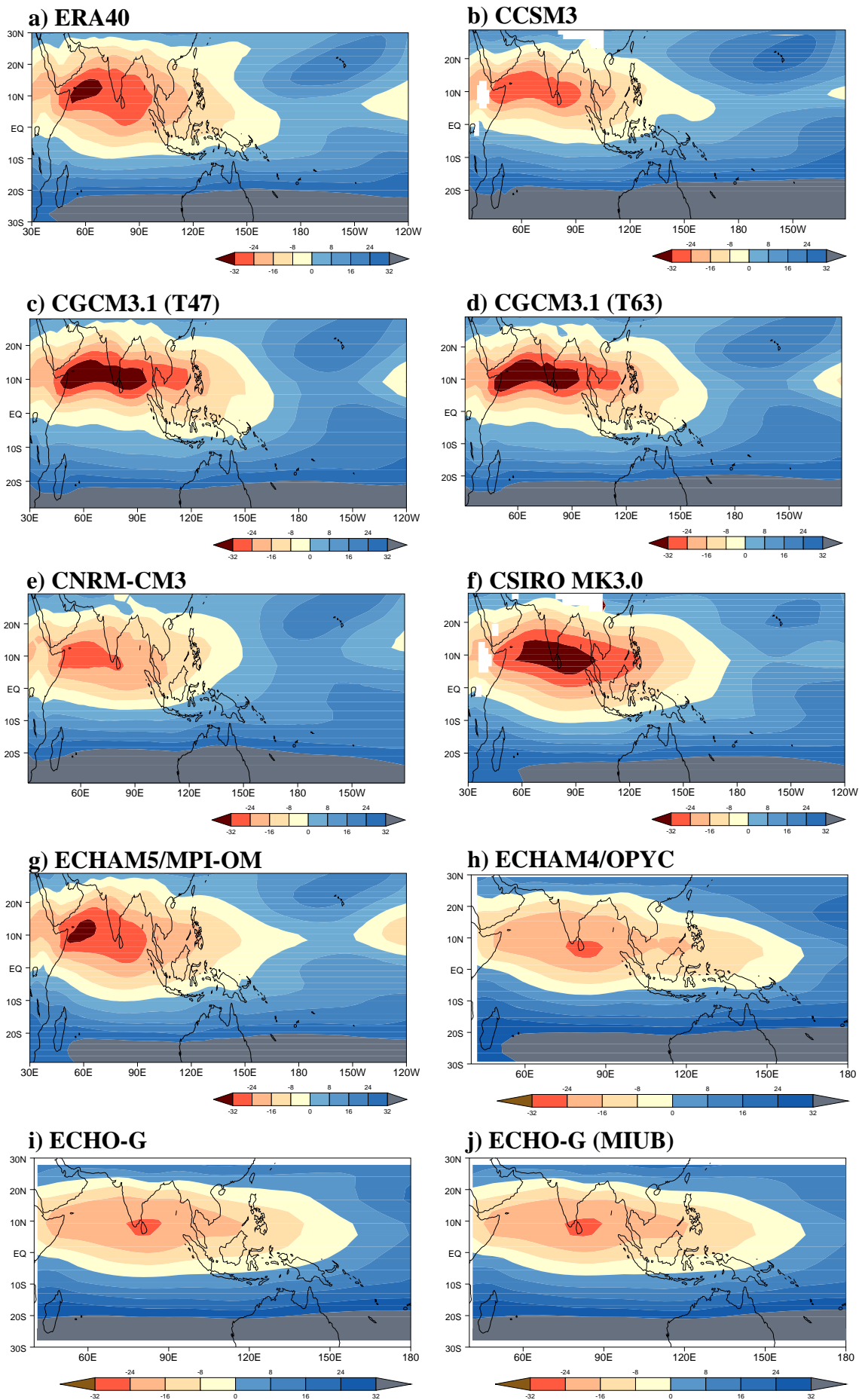
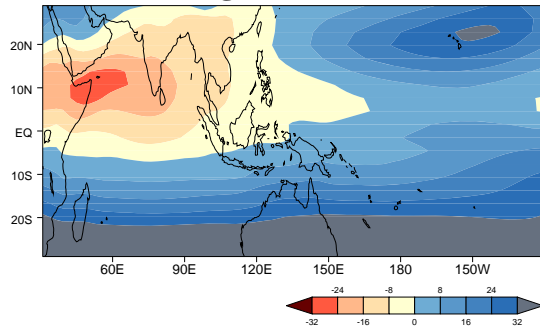
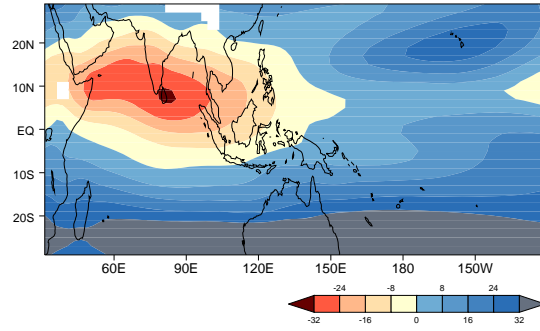


Figure 3

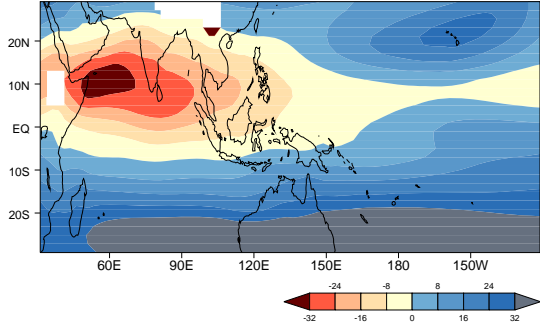
k) FGOALS-g1_0



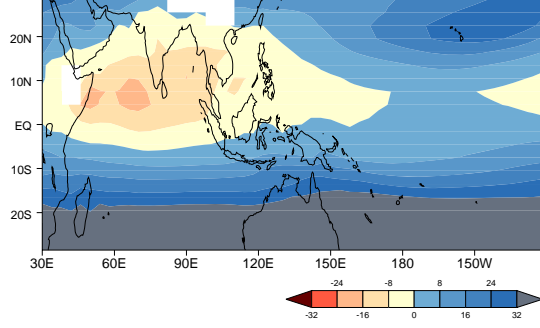
d) GFDL-CM2.0



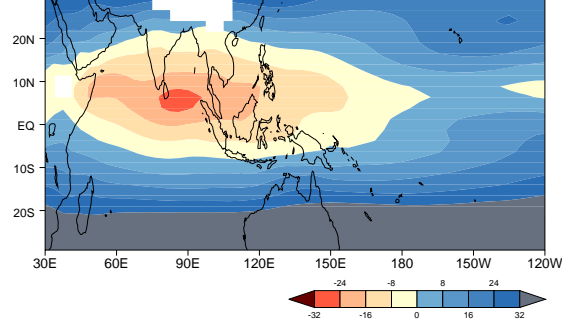
m) GFDL-CM2.1



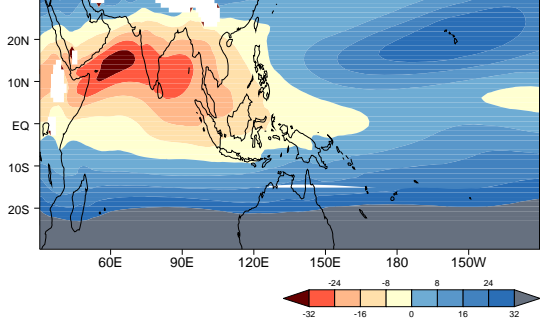
n) GISS-AOM



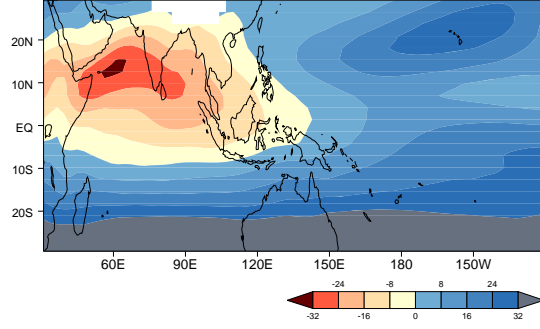
o) IPSL-CM4



p) MIROC3.2 (hires)



q) MIROC3.2 (medres)



r) MRI-CGCM2.3.2

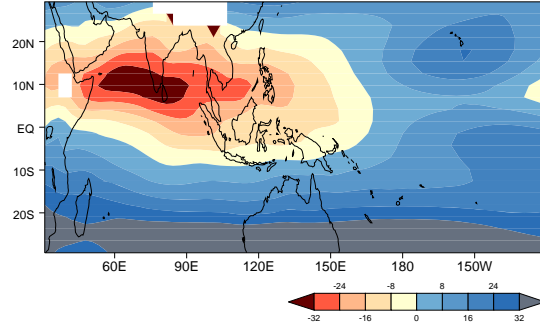


Figure 3 (con't)

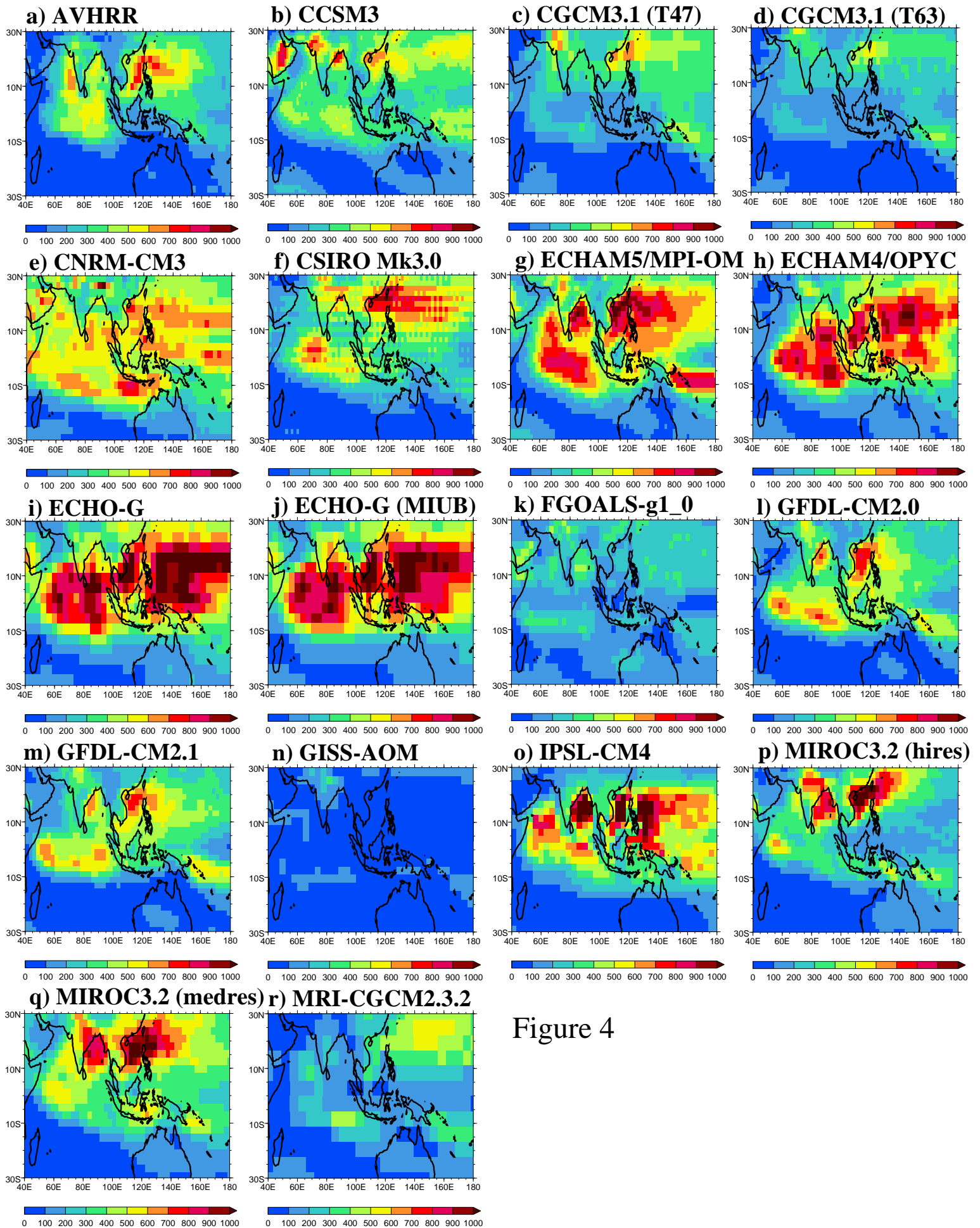


Figure 4

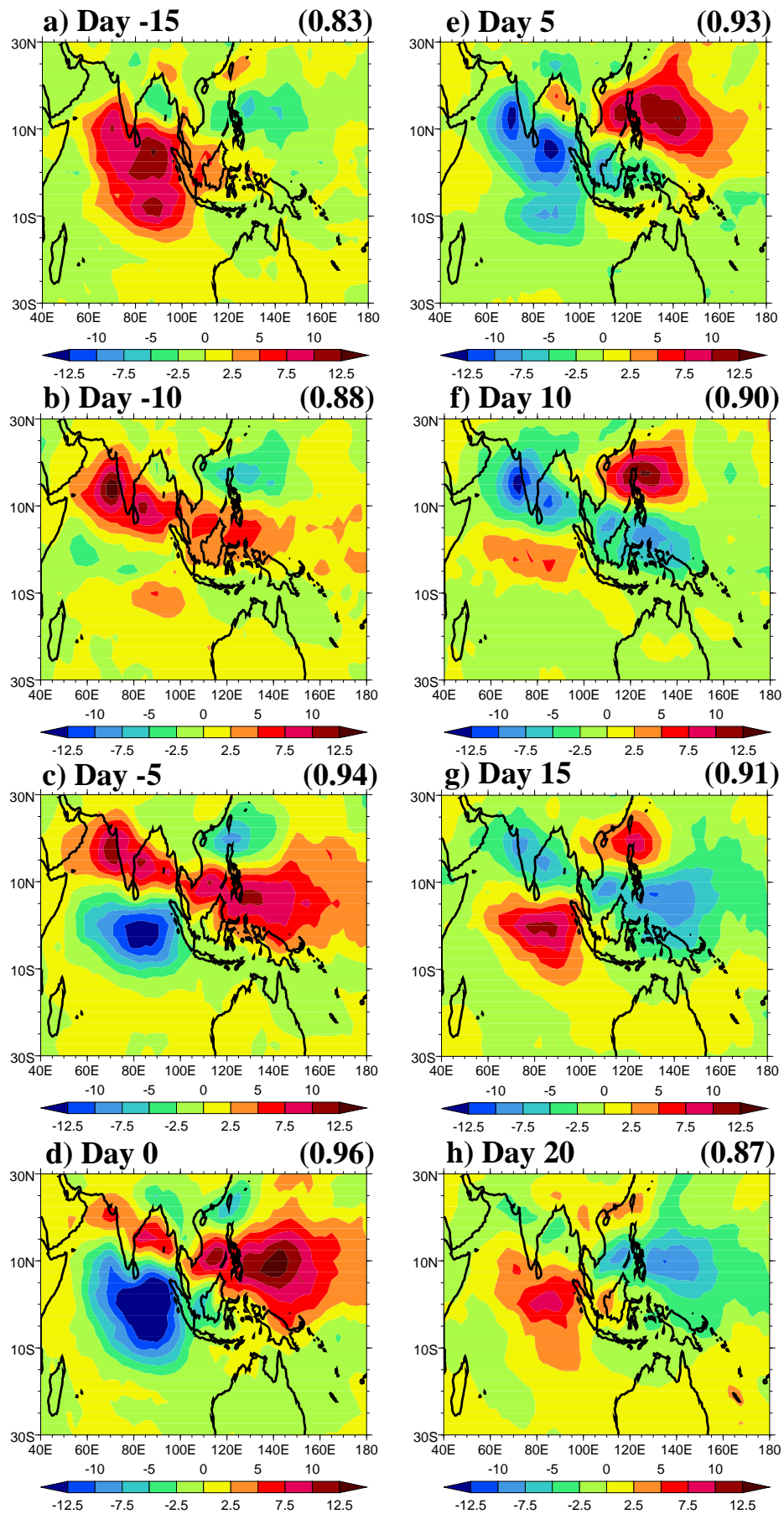
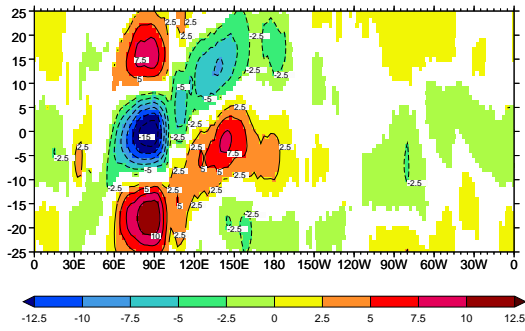


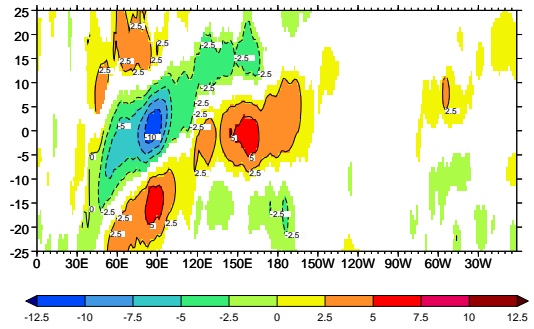
Figure 5

5°N-5°S

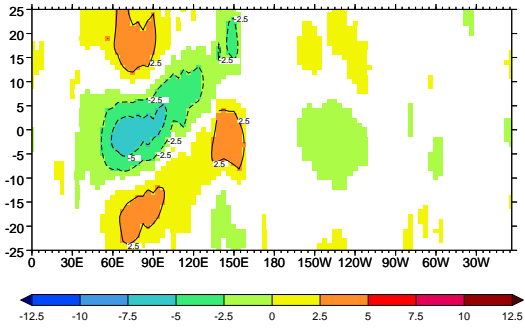
a) AVHRR



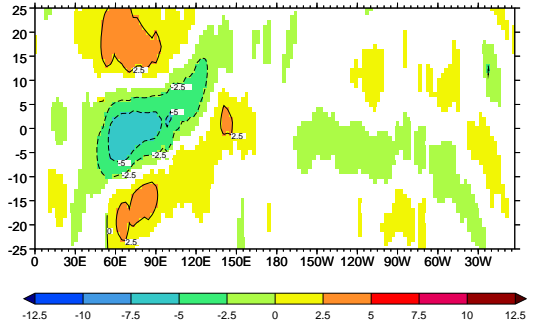
b) CCSM3



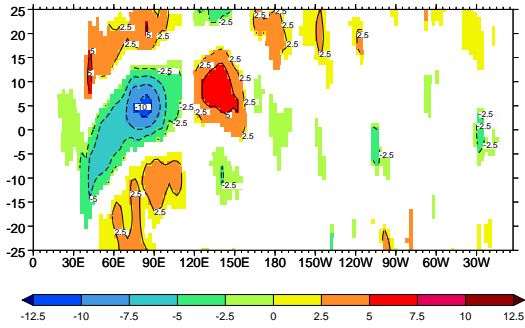
c) CGCM3.1 (T47)



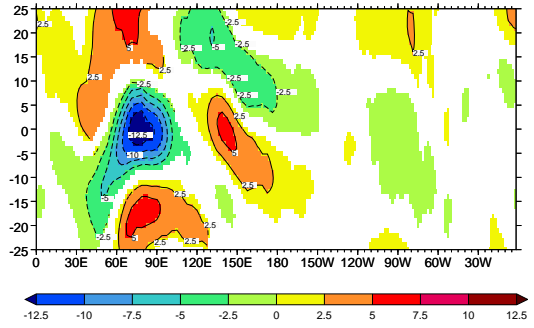
d) CGCM3.1 (T63)



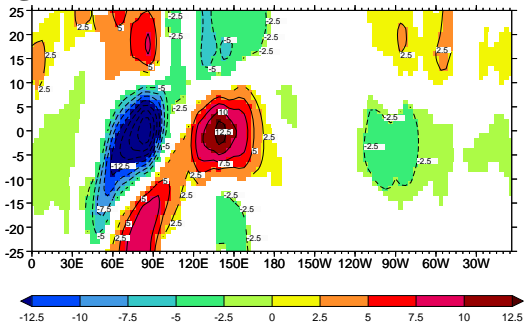
e) CNRM-CM3



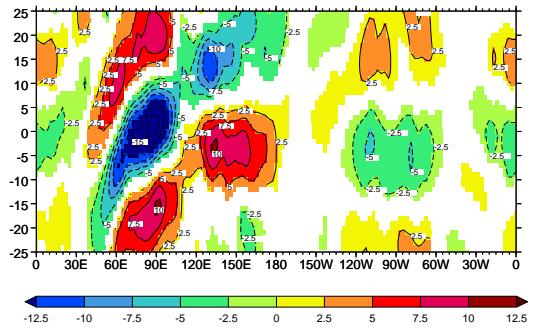
f) CSIRO MK3.0



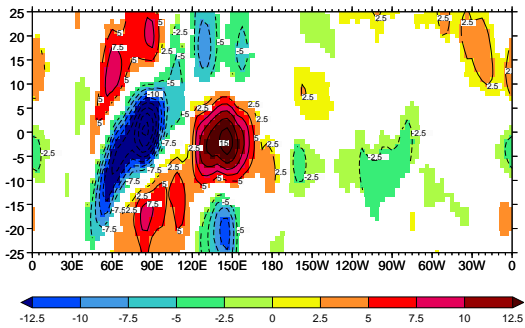
g) ECHAM5/MPI-OM



h) ECHAM4/OPYC



i) ECHO-G



j) ECHO-G (MIUB)

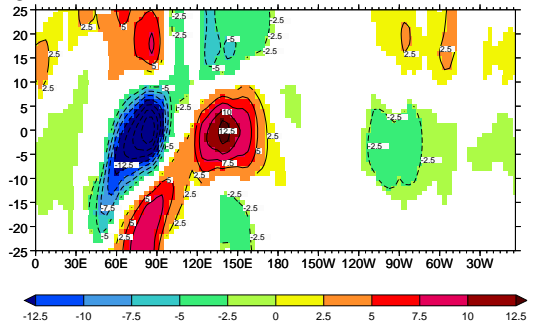
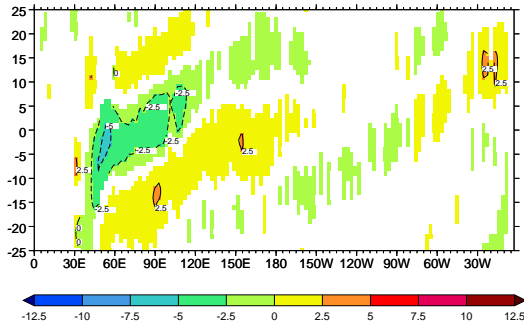


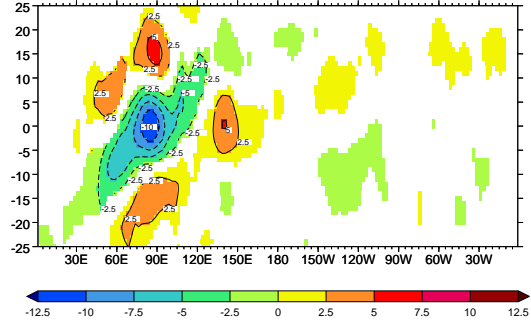
Figure 6

5°N-5°S

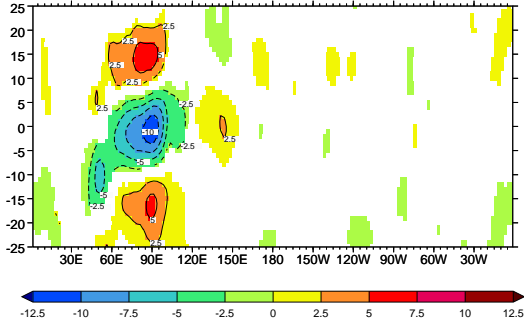
k) FGOALS-g1_0



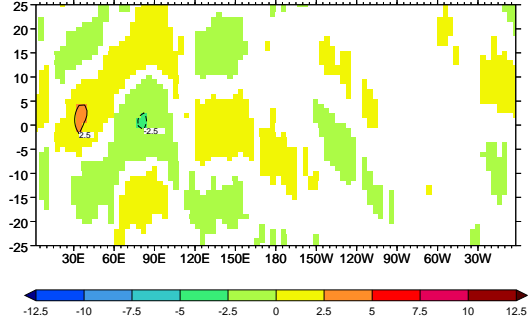
l) GFDL-CM2.0



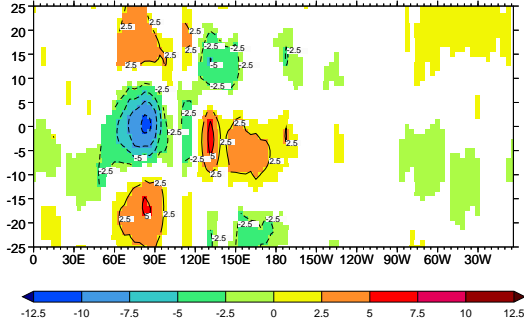
m) GFDL-CM2.1



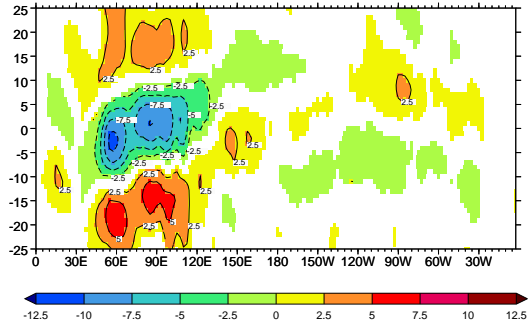
n) GISS-AOM



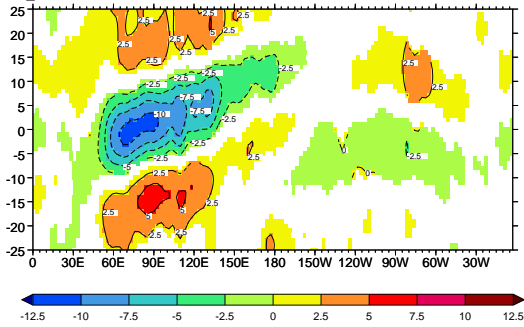
o) IPSL-CM4



p) MIROC3.2 (hires)



q) MIROC3.2 (medres)



r) MRI-CGCM2.3.2

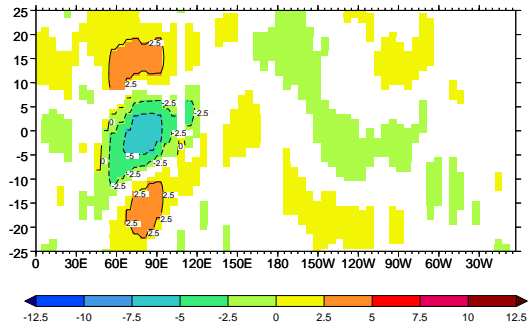


Figure 6 (con't)

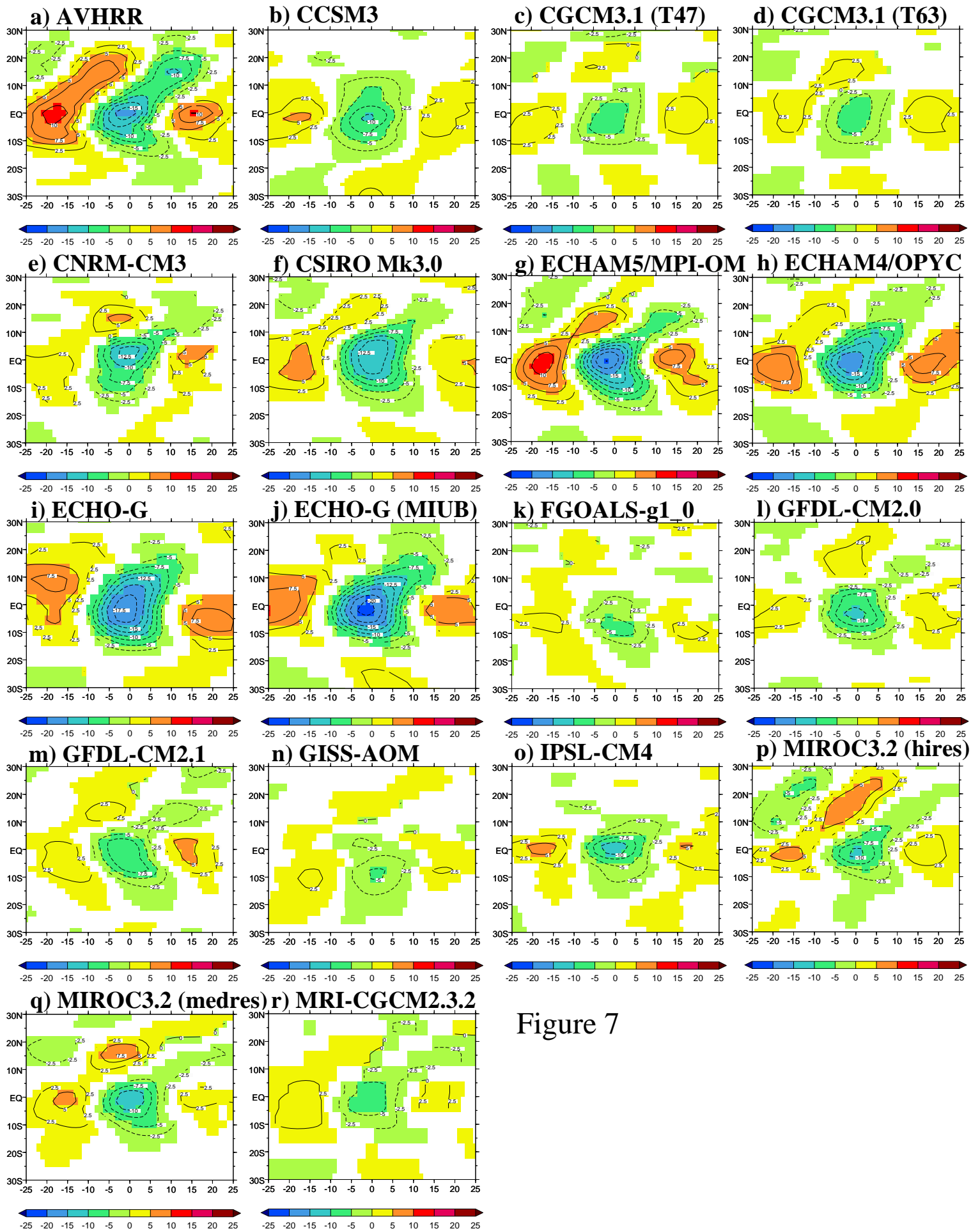
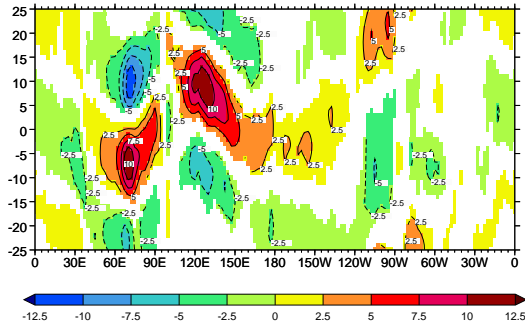


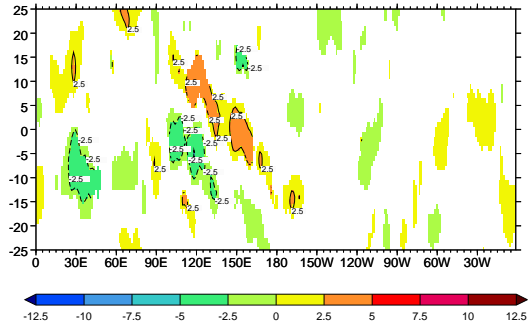
Figure 7

15°N-20°N

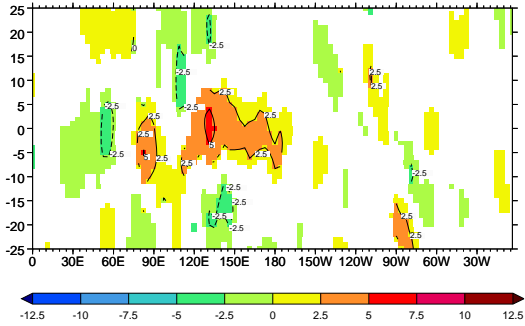
a) AVHRR



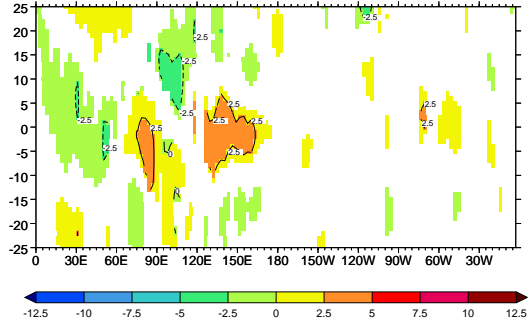
b) CCSM3



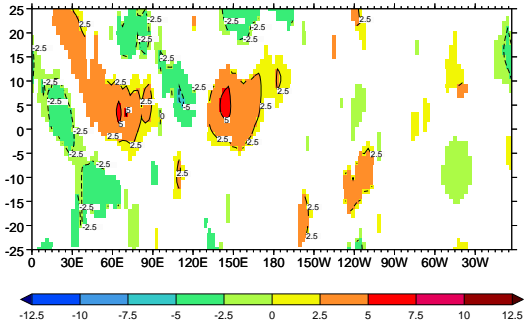
c) CGCM3.1 (T47)



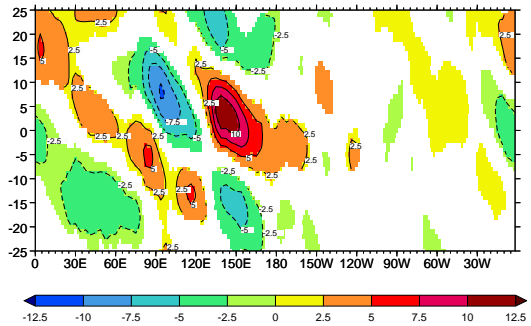
d) CGCM3.1 (T63)



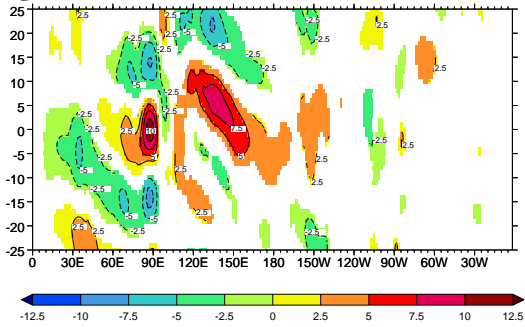
e) CNRM-CM3



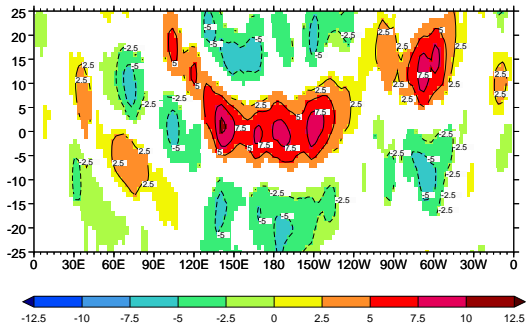
f) CSIRO MK3.0



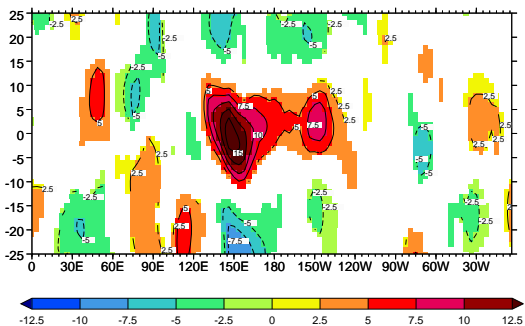
g) ECHAM5/MPI-OM



h) ECHAM4/OPYC



i) ECHO-G



j) ECHO-G (MIUB)

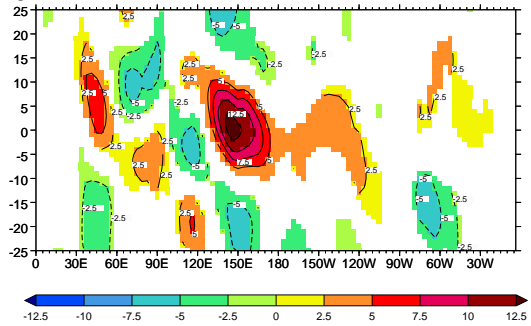
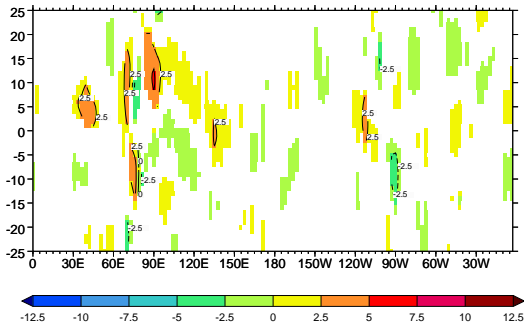


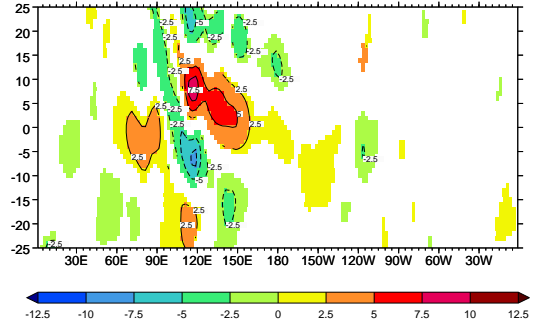
Figure 8

15°N-20°N

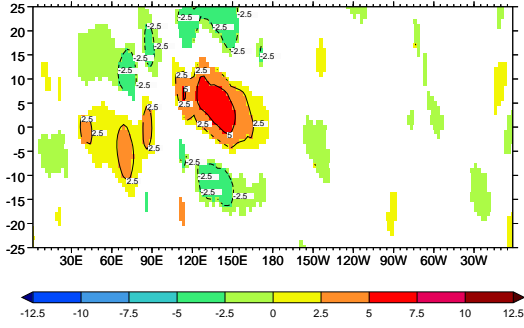
k) FGOALS-g1_0



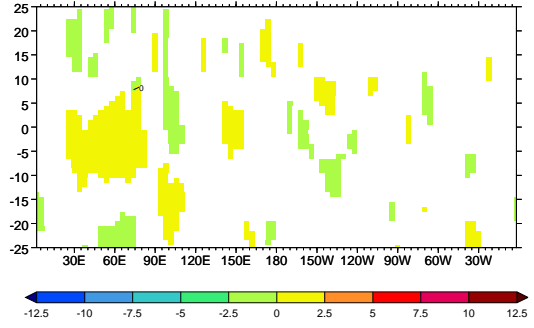
l) GFDL-CM2.0



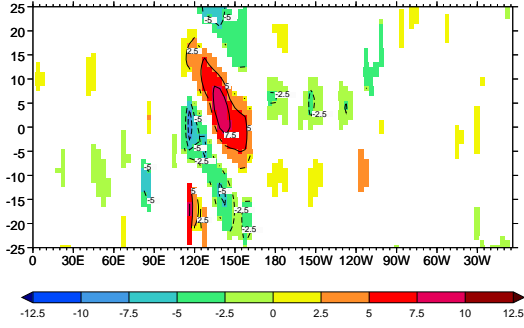
m) GFDL-CM2.1



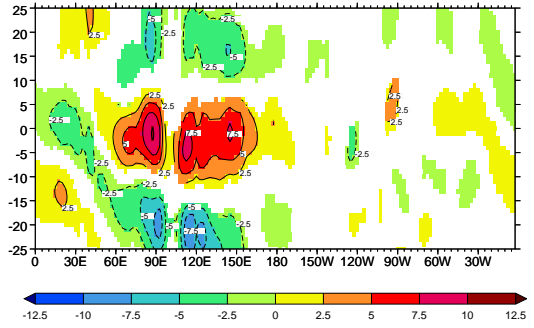
n) GISS-AOM



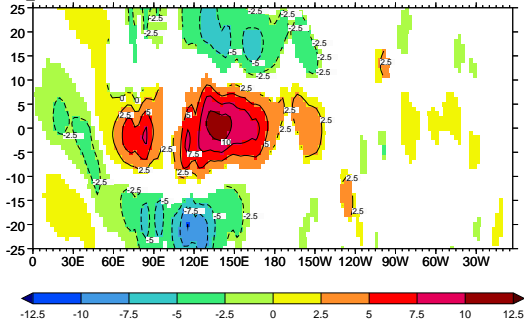
o) IPSL-CM4



p) MIROC3.2 (hires)



q) MIROC3.2 (medres)



r) MRI-CGCM2.3.2

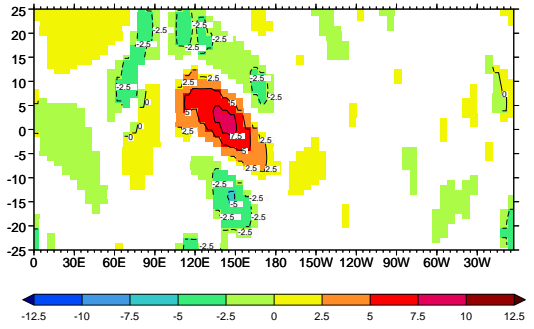


Figure 8 (con't)

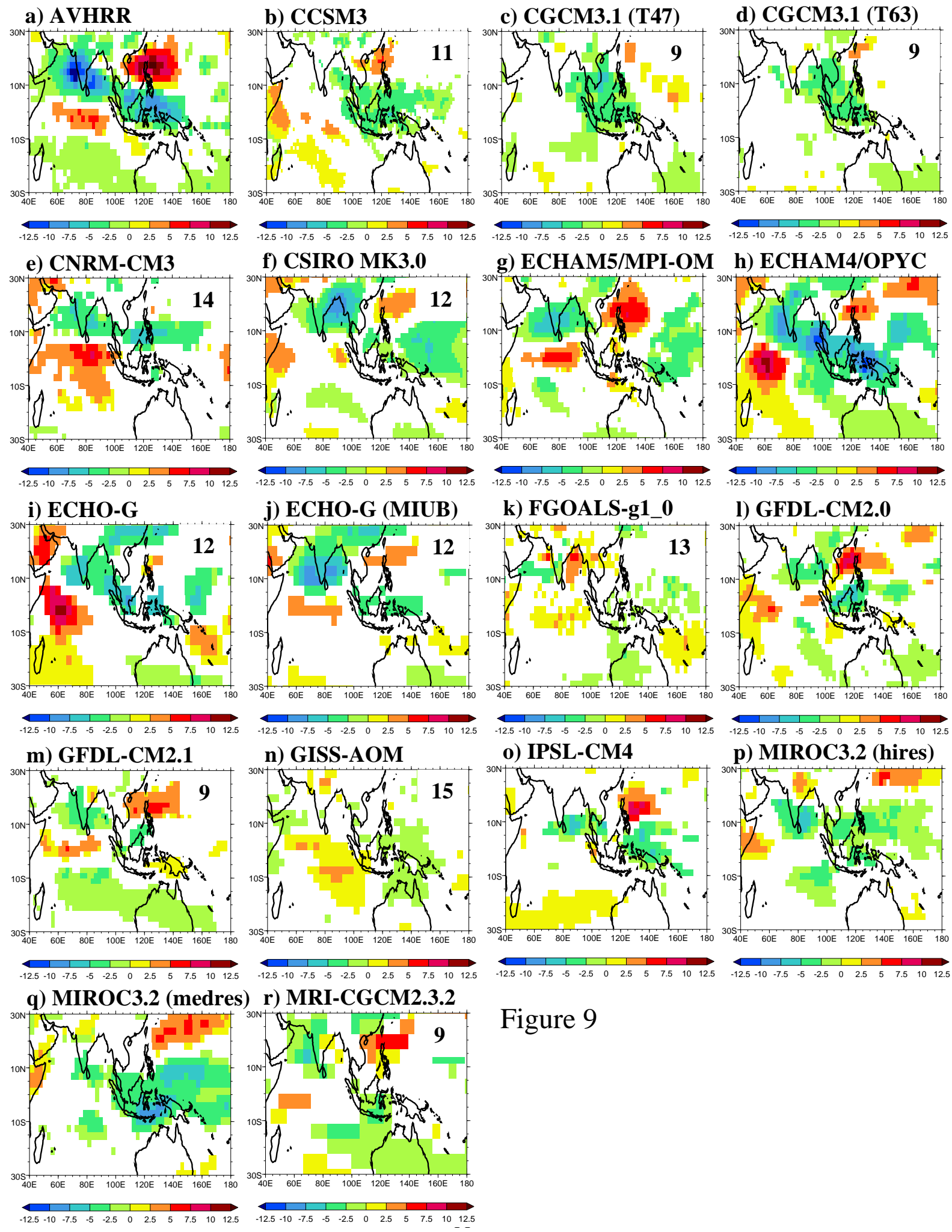


Figure 9

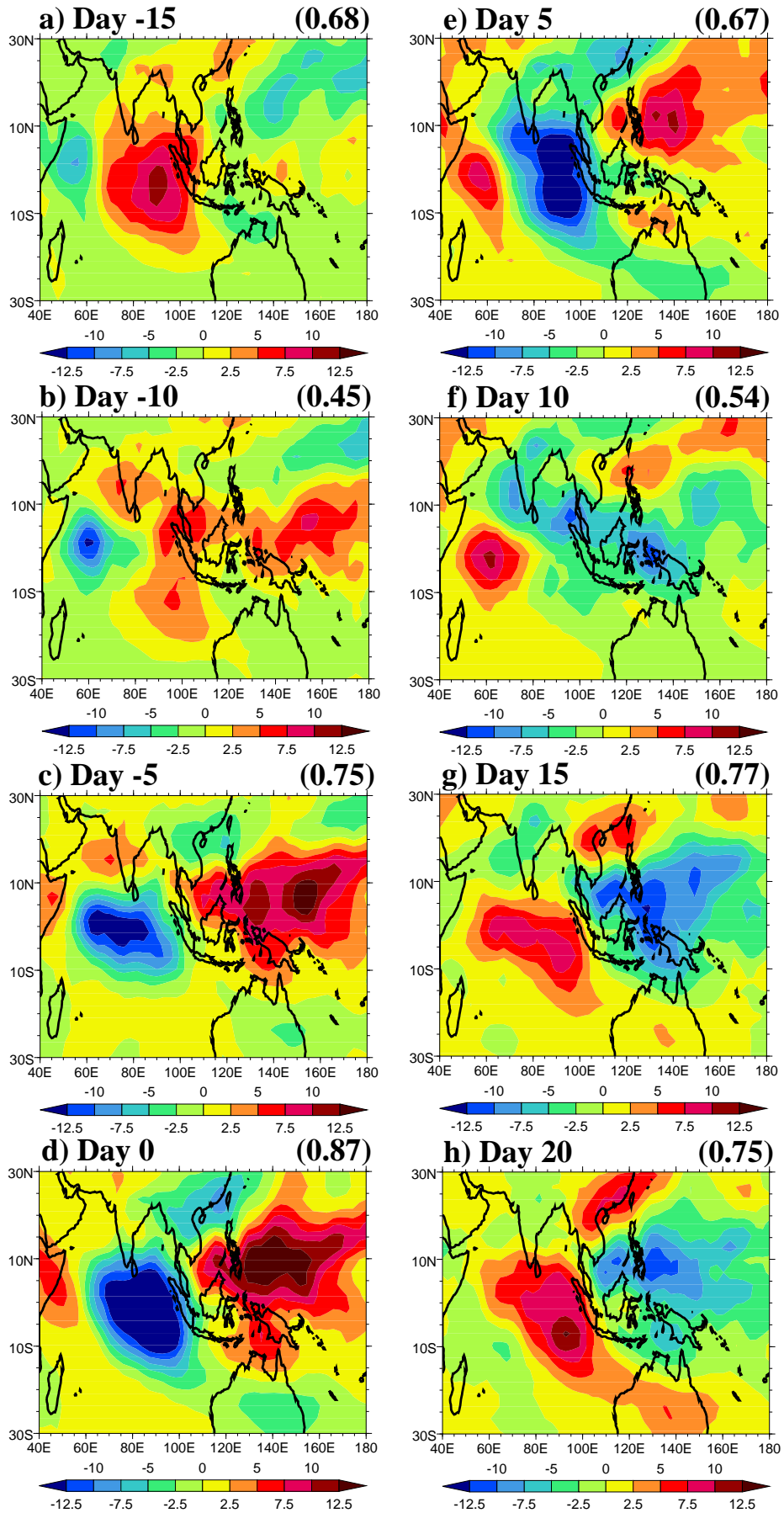


Figure 10

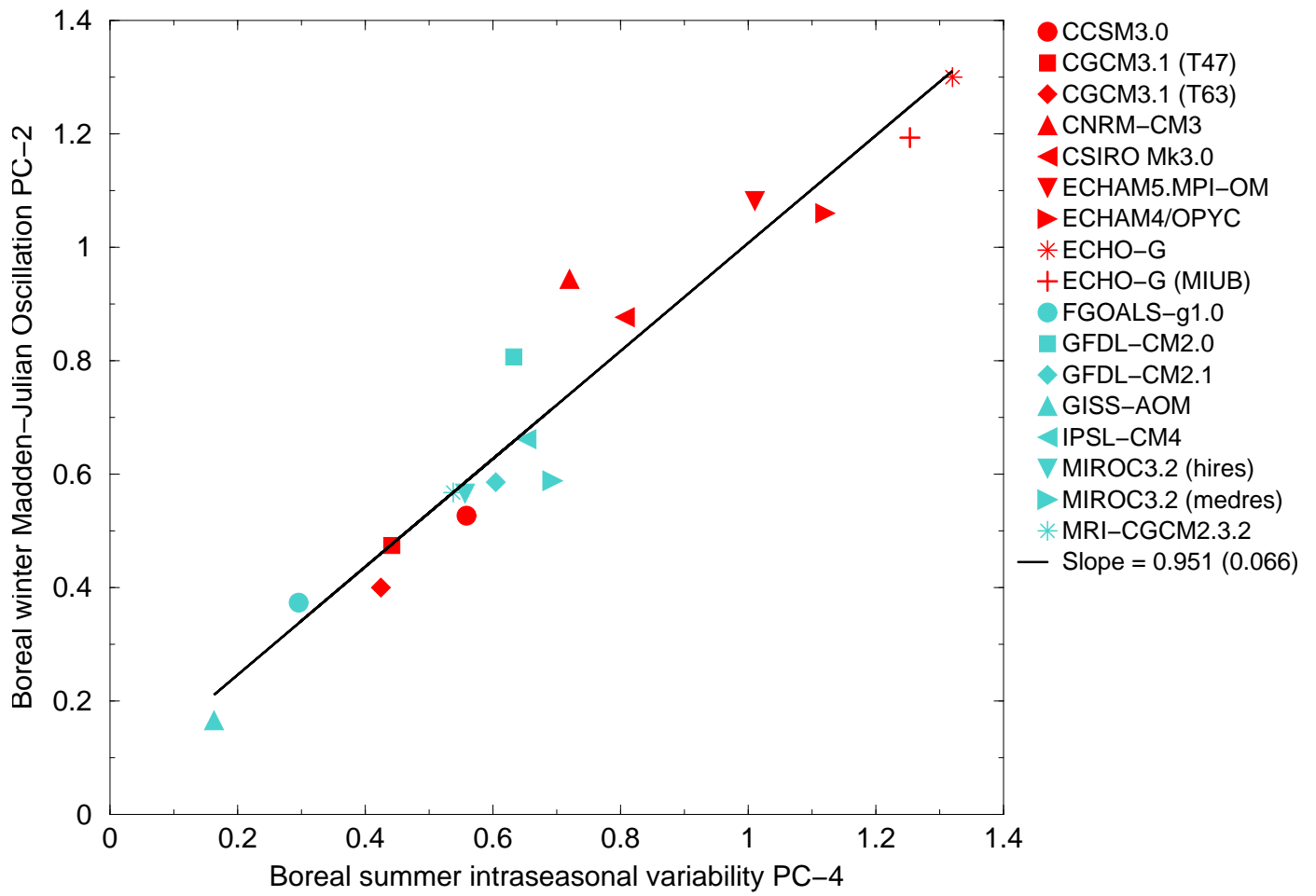


Figure 11